Centre of Studies and Activities for Space Giuseppe Colombo "CISAS"

SPACE NAVIGATION WITH OPTICAL PULSARS

PhD Candidate   *Supervisor*

Samuele Larese De Pasqua   **Prof. Giampiero Naletto**

Co-supervisor

Dr. Paolo Zoccarato

PhD Course: Sciences, Technologies and Measurements for Space

Curriculum: Sciences and Technologies for Aeronautics and Satellite Applications

Coordinator: Prof. Francesco Picano

Series: 36th

Abstract

Deep-space navigation, thus far, has strongly relied on ground segments. Nevertheless, the positioning accuracy of ground-based navigation systems decreases with the distance from the Earth, significantly increasing the positioning uncertainty for interplanetary missions. Furthermore, ground-based navigation systems require extensive ground operations, and their limited bandwidth could lead to a point of full utilization in the future.

The aim of this Thesis is to introduce - for the first time ever - the concept of Space Navigation by Optical Pulsars, a novel technology which aims at overcoming the limits of ground-based navigation systems and those of the already proposed X-ray pulsar-based NAVigation and timing systems. This Thesis presents, first, an introduction to autonomous satellite navigation, highlighting the benefits pulsars could bring. Then, the physical and timing properties of optical pulsars are presented, investigating on the timing techniques allowing to reconstruct, process and make use of a pulsar signal, leading to a position (and velocity) estimation. Finally, the Thesis reports the design for the proposed optical payload and the orbit determination performance of the system, investigating also an on-board optical pulsar-based time synchronization.

Contents

Chapter 1

Introduction

Space navigation, to date, has relied widely on Earth-based navigation systems. Spacecraft in Low Earth Orbits (LEO), for instance, can rely on Global Navigation Satellite Systems (GNSS) for navigation. On the other hand, if the spacecraft altitude exceeds a threshold of approximately 20000 km, radiometric positioning techniques are mostly used [1]. This is done by means of wide networks of radio antennas, e.g. ESA's European Space Tracking (ES-TRACK) and NASA's Deep Space Network (DSN). An angular precision of about 10 nrad is achievable using the DSN, corresponding to a positioning accuracy (linearly decreasing as a function of the distance) of about 1.5 km at one astronomical unit from Earth [2]. Although accurate radial position can be determined using radiometric techniques, it requires extensive ground operations, hence arising the necessity of human intervention for an increasing number of space missions. Furthermore, the limited bandwidth of ground segments could lead to a point of full utilization, with no room to support additional navigating spacecraft.

This Thesis presents - for the first time - the concept of Space Navigation by Optical Pulsars (SNOP). Driven by the extremely stable optical emissions of pulsars, SNOP systems aim at overcoming the limits and the accuracy of current ground and pulsar-based navigation systems, increasing autonomy and providing a positioning accuracy which is theoretically independent of

the distance from the Earth [3].

The idea of exploiting pulsar signals for space navigation dates back to the 70's - soon after their first observations - when Downs [4] proposed for the first time the use of pulsating sources for interplanetary missions. Although pulsars are usually discovered in radio bands, the dimensions of an antenna to detect pulsating radio signals would be impracticable for any spacecraft [5]. Furthermore, because of the low signal intensity of radio pulsars, long observation times are needed to obtain a sufficiently high signal-to-noise ratio (SNR) [6]. Consequently, a large number of feasibility studies, research and in-orbit demonstrations have been carried out considering X-ray pulsars ([6], [7], [8], [9], [10], [11]) (hence the acronym XNAV, X-ray pulsar-based NAVigation and timing), proving the suitability of these sources for navigation. Two in-orbit demonstrations have been carried out testing XNAV systems in space. The first was performed by the NASA's Station Explorer for X-Ray Timing and Navigation (SEXTANT), mounted on the International Space Station (ISS) [11]. SEXTANT was able to pinpoint the ISS position with an accuracy better than 10 km (one-sigma) within two days. The second demonstration regarded the Hard X-ray Modulation Telescope (HXMT), providing a positioning accuracy of about 10 km (three-sigma) after five days of observations [7]. Nevertheless, none of the two demonstrations was solely made for navigation purposes, leading to an increased system complexity. In fact, the instrumentation proposed in [7] has a total geometric area of 5000 sq.cm with 3 X-ray telescopes while in [11] the proposed system is made of 56 X-ray telescopes, with a total effective area greater than 2000 sq.cm. In [12], they investigated the possibility of drastically reducing the size of an XNAV payload, but at the expense of longer observations.

On the other hand, in [8] and [9] they estimated the positioning accuracy of an XNAV system, claiming that a theoretical accuracy of 100-300 m (one-sigma) in three dimensions could be attainable with a detector area of 1 m^2, with initial positioning and velocity errors of 100 m and 0.01 m/s (in each axis) respectively and a measurement error of 35 m after 5000 s of integration

time for the Crab pulsar. These numerical simulations suggest thus the exploitation of pulsars as natural navigation beacons, but also underline that further investigation is needed to approach the indicated theoretical accuracy, in particular on evaluating a measurement accuracy practically achievable. Along with pulsar-based systems, other autonomous navigation systems have been proposed in the literature. Relevant contributions have been made trying to navigate a deep-space satellite exploiting optical images of planets and moons [13] [14], leading to light optical instrumentation suitable also for small-size satellites (e.g. CubeSats).

Mainly because of the low number of pulsars emitting in the optical band, the chance of exploiting their optical emissions for navigation has never been considered. The optical emissions of pulsars show photon fluxes which are comparable to those in the X-ray bands, but the optical contribution of the surrounding nebulae - which constitutes a background noise - is typically more consistent, leading to a lower SNR. However, the capability of an optical system to reject a large fraction of photons coming from the nebula - by narrowing the field-of-view of the system - makes the use of optical pulsars for navigation quite advantageous. In fact, the narrow field-of-view attainable by an optical system leads to a much higher SNR with respect to that attained by the proposed XNAV systems - where the whole nebula affects the signal acquisition - while also reducing the payload weight, size, power and cost.

The Thesis is organized as follows. Chapter 2 introduces the limits of ground-based navigation systems, highlighting the benefits pulsars could bring. Chapter 3 provides an introduction to (optical) pulsars, describing their main properties and limits for their exploitation in a navigation system. Chapter 4 introduces the concept of pulsar navigation, pointing out the advantages derived by the adoption of optical pulsars. Chapter 5 reports the signal models for the candidate optical targets, discussing the achievable positioning accuracy along their line-of-sight directions. Chapter 6 presents the possibility of estimating the satellite orbital parameters and its on-board clock error starting from optical pulsar measurements. Chapter 7 presents

a first optical design for the navigation payload. Chapter 8 introduces and describes the software developed for performing the simulations. Finally, Chapter 9 presents a set of experimental and simulation results.

Chapter 2

Spacecraft Navigation

2.1 Earth-based Navigation

Most of deep space operations, thus far, have relied widely on Earth-based navigation methods for absolute position determination [6]. Although a ground based tracking system has the advantage of not requiring an active hardware on the spacecraft itself, it does need extensive ground operations and careful analysis of the measured data in an electromagnetically noisy background environment. Moreover, as a spacecraft moves further away from Earth, its position estimation error increases linearly if a radar-based navigation system is used [16]. Even if precise information of the radar station and solar system objects position is available, the transmitted radar beam, along with the reflected signal, travels in a cone of uncertainty, degrading the position knowledge of the vehicles as a linear function of distance.

Alternatively, many space vehicles travelling into deep space employ active transmitters for orbit determination purposes. The spacecraft receives a ping from an observation station on Earth and re-transmits the signal back to Earth. Then, the radial velocity is measured at the receiving station by measuring the Doppler frequency of the transmitted signal. Although some improvements are achieved in spacecraft navigation utilizing such systems, this method still has errors that increase with distance.

To obtain accurate absolute navigation solutions for deep space missions, a combination of Earth-based radar ranging and on-vehicle planet imaging is usually required. However, processing video images requires additional devices and computations. Imaging processing requires also the vehicles to be sufficiently close to the planets, hence limiting the usage of such techniques to a restricted set of space missions.

The current spacecraft navigation systems depend mainly on the mission duration and the altitude above the Earth. For spacecrafts orbiting in LEO, GNSS such as Galileo and Global Positioning System (GPS) can be used for position determination. In these cases, the positioning accuracy depends on various factors, e.g. if the spacecraft uses real-time or post-processing position determination techniques or if a wider range of GNSS frequencies is used. To date, the achievable accuracy of the position determination for real-time systems can be ideally of the order of 10 cm [17] [18]. Other examples of such systems are Russia's GLONASS (GLObal Navigation Satellite System) and China's BeiDou. These methods allow to determine the position of a spacecraft with a maximum altitude (with respect to the Earth surface) of about 24000 km.

On the other hand, examples of deep-space navigation systems are DSN and ESTRACK. DSN, for instance, consists of three communication facilities placed at $\sim 120°$ apart around the world: at Goldstone, in California's Mojave desert, near Madrid, Spain, and near Canberra in Australia. This strategic placement permits constant observation of a spacecraft as the Earth rotates and makes the DSN the largest and most sensitive scientific telecommunications systems in the world.

To date, the highest orbit determination accuracy for a deep space mission has been achieved by the Mercury Orbiter Radio Science Experiment (MORE) on board of the ESA/JAXA BepiColombo mission. Making use of range and Doppler measurements from DSN and ESTRACK, MORE aims at performing an orbit determination by means of a two-way coherent radio links system, working in two different radio bands (X and Ka) to calibrate

path delay fluctuations induced on the signal's phase by the solar plasma [19]. The design accuracy of the radio tracking data was 0.004 mm/s (at 1000 s integration time) for range-rate measurements and 20 cm for range (at a few seconds of integration time). In tracking passes with favorable weather conditions, range-rate measurements attained an average accuracy of 0.01 mm/s at 60 s integration time. Data from 20 to 24 May 2019 were combined in a multi-pass analysis to test the link stability on a longer timescale. MORE proved thus the extremely high accuracy Earth-based navigation systems can achieve in the deep space. Nevertheless, such an accuracy is reached thanks to dedicated radio links which strongly rely on ground stations availability and, as in the case of MORE, atmospheric conditions.

2.2 Autonomous Navigation with Pulsars

The limits of Earth-based navigation systems make autonomous navigation quite attractive the future of deep-space exploration. The exploitation of celestial objects for autonomous navigation has always caught the attention of space agencies, and among the natural sources able to provide a spacecraft with hints on its position, pulsars seem to be the most promising ones. In fact, pulsars emit periodic radiation and can be exploited everywhere in the solar system (and beyond), unlike other local navigation techniques (such as Light Detection and Ranging systems). The idea of using pulsars as natural navigation beacons dates back to the 70's, soon after their first observations, when Downs (1974) proposed for the first time the use of pulsating sources for interplanetary missions. Taking advantage of the extremely periodic pulses of these stars, Downs proposed first to use pulsars radio emission, claiming that a positioning accuracy of about 1500 km could be achieved after 24 hours of observation time.

Although pulsars are usually observed and discovered in the radio band, the dimension of a spacecraft antenna to navigate with pulsars at these long wavelengths would be of the order of 150 m^2 [5], impracticable for space mis-

sions. As a matter of fact, for most space missions, large antennas highly impact the design and cost of the operation. Furthermore, because of neighbouring sources that emit in radio bands and also low signal intensity of radio pulsars, long observation times are needed to obtain a sufficiently high SNR [6]. For this reasons, a large number of feasibility studies, research, simulations and in-orbit demonstrations have been carried out considering X-ray millisecond pulsars [6][7][8][9][10][11]. X-ray millisecond pulsars are also the most stable among all the kinds of pulsars, ideally providing a higher positioning accuracy.

The idea of using optical pulsars for navigation has not been considered yet. The reason why optical pulsars had not been studied for navigation is their very low number [21] and the neglected possibility of limiting the nebular noise by means of a narrow field-of-view optical system. This Thesis shows that an optical system able to filter the nebular background can lead to a much higher SNR with respect to that achievable in the X-ray band, leading to shorter observation times and smaller telescopes.

2.2.1 In-Orbit Demonstrations

To date, pulsar navigation systems have already been tested in orbit. In this subsection, the main results are reported.

- ARGOS (*Advanced Research and Global Observation Satellite*, 1999): first experiment of pulsar navigation [11]. ARGOS primarily conducted feasibility assessment exercises rather than full operational demonstrations. The Crab pulsar was observed and its pulse shape was obtained.

- POLAR (2016): a Gamma-Ray Bursts Polarimeter whose aim was to measure the polarization of gamma-ray bursts. Because of its large effective area (about 200 cm^2), the instrument could be used to detect photons from X-ray pulsars and it was used for testing pulsar navigation [52]. The instrument observed the Crab pulsar for 31 days and the positioning accuracy was about 20 km.

- NICER (*Neutron star Interior Composition ExploreR*, 2017): launched on the International Space Station (ISS), NICER consists of 56 identical X-rays telescopes for a total effective area of about 2000 cm^2. Observing five millisecond pulsars, the spacecraft determined its own position with an accuracy of 5 km [11].

- Insight-HXMT (2017): composed by three X-ray telescopes, has an effective area of about 5000 cm^2. Using five-day long observation of the Crab pulsar, position and velocity of the satellite were determined within 10 km and 10 ms^{-1} respectively [7].

Chapter 3

Pulsars

This chapter presents first an introduction to pulsars' history and then describes their physical properties focusing on their creation, emission mechanisms and the classes in which pulsars are categorized.

3.1   History and Discovery

The existence of neutron stars was first proposed by Baade and Zwicky [22], two years after the discovery of the neutron by Chadwick (1932). They suggested that these stars would have had an extremely high density, a short radius and be much more gravitationally bounded with respect to ordinary stars. According to Baade and Zwicky, neutron stars would be formed in supernova explosions, where the extreme pressure exercised in the centre of the explosion would trigger an inverse beta decay, in which electrons and protons are combined to form neutrons and neutrinos. The expected size and mass of a neutron star were calculated by Oppenheimer and Volkov (1939) and they stated these stars would have a radius of about 10 km with a $1.5M\odot$ of mass, where $M\odot$ is the Solar mass [23].

Although the theories about neutron stars seemed to be quiet consolidated, it was necessary to wait until 1967 for a first real observation [24]. The first pulsar, PSR B1919+21 was observed in 1967 by Burnell and Hewish,

who won the Nobel Prize in 1974. The real aim of the research group was to study the scintillation of quasars in the radio band, window that had just been opened to the astronomical exploration. At the beginning, because of the small size of the emitting source and the periodicity of the signal, the source was named Little Green Men 1 (LGM-1), considering the possibility of an extraterrestrial interaction. Soon after, since similar events were detected in different parts of the sky, Hewish and Bell discarded the hypothesis of an extraterrestrial form. The identification of PSR B1919+21 with a neutron star was not immediate and was pointed out by [25]. Knowledge about optical emission of pulsars has been remarkably improved only after the 80's.

Prior to the beginning of the 80's, only two, among the $\sim$500 discovered pulsars had been identified also at optical wavelengths [26]. These two were the Crab (PRS B0531+21969) discovered in 1969 by Cocke [27] and the Vela (PSR B0833-45), discovered by Wallace [28].

3.2   Physical Properties

Pulsars are fast rotating highly magnetized neutron stars emitting beams of broadband electromagnetic radiation. The beams are emitted from the pulsar's magnetic poles along narrow emission cones (Fig. 3.1). Radiation can be observed only when a beam of emission is pointing toward our line of sight [29].

Neutron stars are formed from the collapse of the nucleus of a massive star (of about 8-30$M_\odot$), when its nuclear fuel is exhausted. The binding energy released by the collapse induces a supernova explosion in which the bulk of the progenitor star is expelled into the interstellar medium. At the end of the gravitational collapse, a very compact object with a $\sim$10 km radius and a $\sim$1.5$M_\odot$ mass remains [5]. Due to the collapse, protons and electrons combine to form neutrons; hence the name *neutron star*. The collapsed star is born with an extremely high rotation period due to the angular momentum conservation. For this reason, these sources behave like cosmic lighthouses
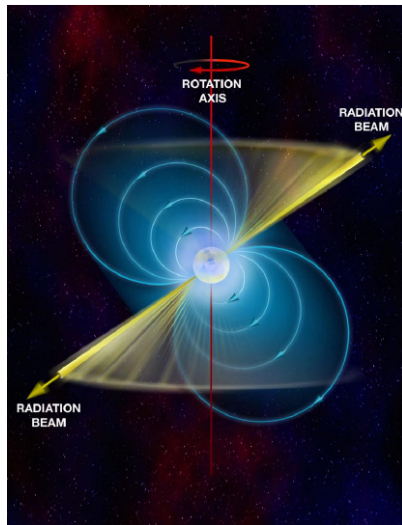
Figure 3.1: Graphical representation of a pulsar. The magnetic dipole axis is not aligned with the rotation axis. Credit: B. Saxton, NRAO/AUI/NSF.

emitting a sequence of regular pulses; hence the name *pulsar*, standing for Pulsating Radio Source.

Pulsars signals have timing stabilities comparable to atomic clocks, mainly because of their isolated environments and very stable moments of inertia. However, some time irregularities have been found upon long term observations [29]. Two kinds of time irregularities have been observed:

- *glitches*: unpredictable changes in the rotational period, interpreted as changes in the pulsar environment or in the neutron star interior. Whenever a glitch occurs, the rotation rate suddenly changes and a period of relaxation follows before pulsar period reaches a stable value [30]. The evolution of the rotational phase of young pulsars is characterized by long relaxation periods following significant glitches, whereas older pulsars show quasi-periodic behaviours with phase modulations on typical timescales between one and ten years [31].

- *timing noise*: pulsars behave as rotating magnetic dipoles that emit energy at the expense of their rotational energy hence decelerating in

time. Therefore, pulsars periods, which range from milliseconds to seconds, increase slowly with time. This phenomenon can be described with the standard pulsar spin-down model, where the predicted phase of the pulsed signal from the $k-$th pulsar at an inertial point - such as the Solar System Barycenter (SSB) - at time instant t can be modeled as [10]

$$\phi_{SSB}^k(t) = \phi_{SSB}^k(T_0) + \nu^k(t - T_0) + \sum_{m=2}^{N} \frac{\nu^{k(m)}(t - T_0)^m}{m!} , \qquad (3.1)$$

where T_0 is the reference epoch (in which the signal phase is assumed to be known), ν^k is the pulsar rotation frequency and ν^{km} is its m-th order time derivative.

The pulsars with the highest rotational stability are the millisecond ones, showing a short spin period $T < 10$ ms and a high rotational stability $dP/dt \simeq 10^{-18}$ - 10^{-21} s/s. However, only two optical pulsars are millisecond pulsars and the contribution of their pulsation to the total signal intensity is very small [34][35][36]. Hence, in pulsar navigation systems (with emphasis on SNOP systems, where no millisecond pulsars are suitable for navigation), pulsar slow-down effects need to be considered on board the satellite, eventually with the support of a ground segment providing these pulsar properties (pulsar ephemeris) as auxiliary data (e.g. those reported in the radio archive at the Jodrell Bank Observatory).

Pulsars are categorized into three different classes:

- *accretion powered pulsars*: binary systems of a normal star and a neutron star in which the latter gains energy and angular momentum by accreting matter from the former. These sources usually emit X-rays and are characterized by an unpredictable evolution of the rotation period. Accretion powered pulsars can be very bright sources but present a non-coherent timing behaviour due to the interaction of the pulsar magnetosphere with the accretion disk.

14

- *magnetars*: isolated, highly magnetized neutron stars. They typically emit X and gamma rays and their timing behaviour is not well determined yet.

- *rotation powered pulsars*: found in isolated or binary systems, are characterized by a broadband emission of radiation, from the radio band to the gamma-rays. The spin period increases as the rotational energy is radiated into the interstellar medium. Rotation powered pulsars are further divided in two classes:

  - ordinary isolated pulsars: most of the rotation powered pulsars are of this kind. They present a period between tens of milliseconds to several seconds.

  - millisecond pulsars: characterized by periods below tens of milliseconds, these pulsars have a significant timing stability and a low spin down rate. Much older than the other pulsars, they are usually found in non-interactive binary systems.

In order to graphically represent pulsars life cycles and timing properties, a P-$\dot{P}$ diagram can be used (Fig. 3.2), where $\dot{P}$ is the time derivative of the rotational period P. Younger pulsars tend to slow down quiet fast, leading to a larger value of $\dot{P}$. In the upper-left part of a P-$\dot{P}$ diagram the youngest pulsars (i.e. the ones which are still associated with their supernova remnants) are found. Older pulsars can be found in the center of the diagram. In the bottom-left part of the diagram millisecond pulsars (i.e. the most stable and oldest pulsars) are found presenting a low $\dot{P}$ value.

3.2.1 Radiation Emission Mechanisms

Pulsars radiation emission mechanisms strongly depend on the age of the neutron star. Radiation emission of young pulsars is synchrotron radiation from relativistic particles which spiral around the magnetic field lines. For
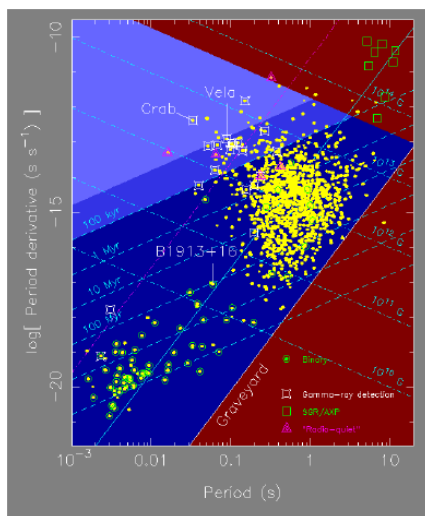
Figure 3.2: P-$\dot{P}$ diagram. The straight lines represent values of constant age and magnetic field. Credit: Jodrell Bank observatory.

middle-aged pulsars instead, radiation emission is synchrotron radiation and thermal radiation from the cooling neutron star surface. Often, an arrival time delay between the detection in different electromagnetic bands occurs and this is explained by assuming that emission regions of different spectral bands differ in position. A delay between the radio and the optical measurements has been observed in the Crab pulsar. More precisely, the optical pulse leads the radio one [32]. Furthermore, the detected pulse shapes are different.

3.3   Optical Pulsars

When looking at the signal from a pulsar, it must be considered that, especially in the optical band, the surrounding nebula gives an important contribution to the emitted flux, which has to be taken into account as background noise (Fig. 3.3). In fact, the pulsed component is only a fraction of the emitted radiation and the presence of the nebula could drastically reduce the SNR. However, the nebula contribution can be highly reduced with a narrow

Figure 3.3: The Crab Nebula, which contains the Crab Pulsar (the red star in the center). Image combines optical data from Hubble (in red) and X-ray images from Chandra (in blue). NASA/CXC/ASU/J. Hester et al.

field-of-view system.

The Australia Telescope National Facility (ATNF) radio pulsar catalog counts more than 2800 pulsars. The LAT 4-year Source Catalog (3FGL) gamma-ray pulsar catalog counts about one hundred pulsars. On the other hand, only thirteen known pulsars have optical counterparts (Tab. 3.1). Fig. 3.4 shows the distribution of optical pulsars in the galactic coordinate reference system. Almost all pulsars are at galactic distances: the known optical pulsars are in our galaxy apart from PSR B0540-69, which is in the Large Magellanic Cloud, the closest dwarf galaxy to the Milky Way.

Like in X-ray bands, the Crab pulsar is the source with the highest photon flux. Being used as a calibration candle since its discovery, the Crab pulsar is surely an outlier in performance when it comes to brightness. Therefore, the SNR achievable by observing the Crab pulsar can be reached with other pulsars only by very long observations. This fact is already evident by looking at Tab. 3.1, since the reported apparent magnitude is directly linked to the photon fluxes estimated on ground. The three brightest optical pulsars are the Crab, Vela and PSR B0540-69 pulsars and thus, these are the best optical pulsars for navigation. It should be noticed, however, that the low photon fluxes of the other optical pulsars will make their exploitation rather hard,
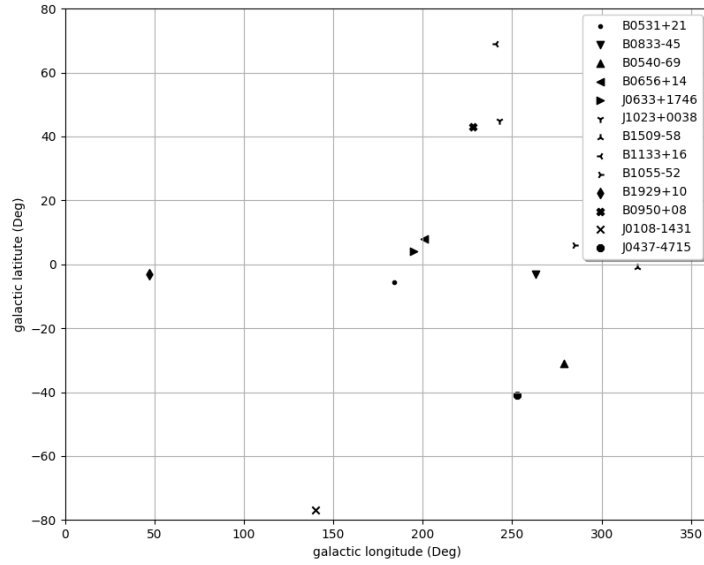
Figure 3.4: Distribution of optical pulsars in galactic coordinates.

Table 3.1: Optical Pulsars' properties.

Name	Period (s)	Period Derivative (s/s)	Apparent Magnitude	Galactic Longitude (deg)	Galactic Latitude (deg)
B0531+21	0.033	4.21E-13	16.6	184.558	-5.784
B0833-45	0.089	1.25E-13	23.6	263.552	-2.787
B0540-69	0.051	4.79E-13	22.0	279.717	-31.516
B0656+14	0.385	5.49E-14	25	201.108	8.258
J0633+1746	0.237	1.09E-14	25.5	195.134	4.266
J1023+0038	0.002	6.93E-21	n.a.	243.490	45.782
B1509-58	0.089	1.25E-13	25.7	320.32	-1.162
B1133+16	1.188	3.73E-15	28	241.895	69.196
B1055-52	0.197	5.83E-15	24.9	285.984	6.649
B1929+10	0.151	1.53E-12	25.6	47.382	-3.884
B0950+08	0.226	1.16E-15	27.1	228.908	43.697
J0108-1431	0.807	7.70E-17	26.4	140.930	-76.810
J0437-4715	0.006	5.73E-20	26.4	253.394	-41.963

requiring very long observations.

Fig. 3.5 shows four examples of apertures which can be adopted while observing the Crab pulsar. The narrower the aperture, the larger the amount of rejected nebular photons. Tab. 3.2 reports the photon fluxes (expressed in photons cm^{-2} s^{-1}) for the three brightest optical pulsars in both the optical (1.5-3 eV) and soft X-ray (0.2-10 keV) bands, ranges which are typically considered for pulsar observations (the fluxes have been retrieved from [33], [37] and [38]).
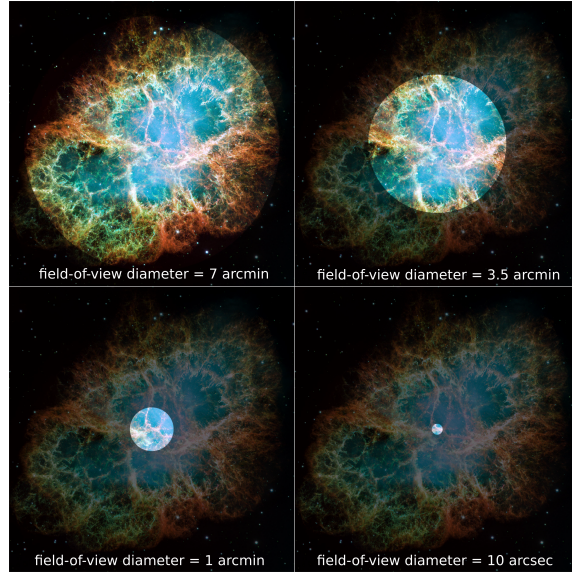
Figure 3.5: Crab pulsar nebula observed with various apertures.

Table 3.2: Photon fluxes (photons cm^{-2} s^{-1}) for the three brightest optical pulsars.

Pulsar	Pulsar (Optical)	Pulsar (X-ray)	Nebula (Optical)	Nebula (X-ray)
Crab	0.75	0.77	7692	11.33
PSRB0540-69	0.0017	0.00079	n.a.	0.00501
Vela	0.001	0.01	n.a.	n.a.

The performance of a pulsar-based navigation system is found in the SNR of the received pulsar signals. The SNR of a light curve depends on the pulsar-over-nebula ratio, which can be defined as ([6])

$$P_r = \frac{N_p}{\sqrt{N_p + N_n}} \tag{3.2}$$

where N_p and N_n are the photon fluxes of the pulsar and of the nebular background respectively, which are assumed to follow a Poisson distribution. Due to the limits of X-ray instrumentation, the field-of-view diameter cannot be arbitrarily reduced and the whole nebula contribution is typically taken into account. Considering the Crab pulsar, the P_r ratio in the X-ray band is of about 0.22, while it is of about 0.0085 in the optical band (considering the whole nebula). Fig. 3.6 shows how P_r can be improved in the optical band, by narrowing the system's field-of-view. The pulsar-over-nebula ratio for the Crab pulsar in the optical band can be higher than 4 if an aperture narrower than 2 arcsec is chosen.
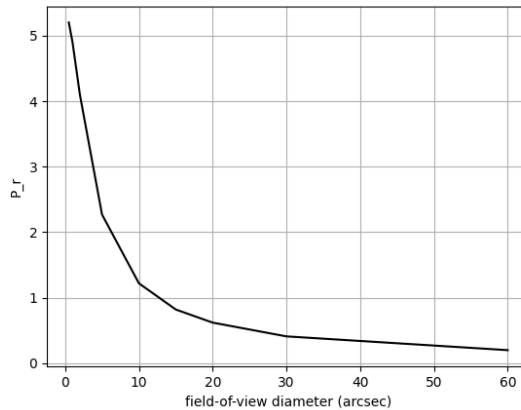

Figure 3.6: Pulsar-over-nebula ratio for the Crab pulsar in the optical band.

It should be noticed, however, that a narrow field-of-view impose a very stable attitude control system to the spacecraft. On the other hand, the attitude control system requirements are less demanding in XNAV systems, despite of a larger amount of nebular photons impinging onto the detector.

20

Chapter 4

Pulsar Navigation

4.1   Pulsar Navigation Concept

Pulsar navigation is based on the principle of baseline estimation from periodic signal interferometry, where phase measurements at two different locations, the SSB and the user telescope reference point, are used to estimate the baseline between them. The pulsar navigation concept, similarly to the GNSS navigation concept, is composed of three navigation segments: the space segment, which is the set of pulsars whose periodic signals are exploited for the interferometry process; the ground segment, which is composed by the optical and radio telescopes on Earth in charge of detecting and disseminating the pulsar timing properties and the phase signal at the SSB (notice that this is the only aid a pulsar-based navigation system needs from Earth); finally, the user segment, which includes all the users receiving the set of information about the pulsar timing properties and SSB phase from the ground segment and measuring their own pulsar signals for estimating their position, velocity and clock error.

Pulsars are distant thousands of light years from the solar system, therefore the pulsar radiation direction can be approximately regarded as a constant vector throughout the solar system. Let $\mathbf{u}_k$ be the unit vector defining the line-of-sight between the spacecraft s and the k-th observed pulsar. As-

suming the SSB to be at the center of the considered reference frame, the light travel time in vacuum τ^k between the satellite position $\mathbf{r}_s$ and the SSB at epoch t_j is given by

$$\tau_j^k = \frac{\mathbf{u_k}^\mathsf{T} \cdot \mathbf{r}_s\left(t_j\right)}{c}\,,\tag{4.1}$$

where $\mathbf{u_k}^\mathsf{T} \cdot \mathbf{r}_s$ is the projection of the satellite position along the line-of-sight direction of the pulsar (where T denotes the transpose operator) and c is the speed of light.
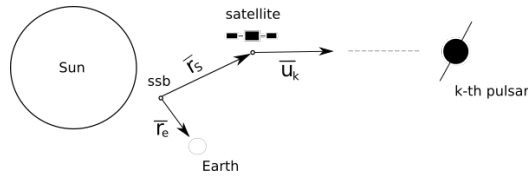

Figure 4.1: Visualization of the baseline interferometry concept for pulsar navigation.

The measurement at the basis of pulsar navigation is the detection of the pulsar photons. Pulsars are faint objects and more than one pulsar period is required to reconstruct the pulsed signal. A process which can be exploited to reconstruct a pulsar light curve starting from the photons' Time of Arrival (ToA)[1] measurements is *epoch folding*. Epoch folding is a technique which is typically used in astronomy to estimate the period of a pulsating source. In this process, all of the collected ToAs are folded back into a single time interval equal to one pulsar period, hence increasing the signal statistics (Fig. 4.2). In pulsar navigation, the epoch folding technique is not used to estimate the pulsar period - which is assumed to be known at the user - but rather to estimate the phase of the reconstructed light curve. Moreover, the epoch folding technique requires a phase shift of the successive pulsar periods received during the signal integration to avoid artifacts due to Doppler effects because of the telescope motion.

---

[1]In pulsar astronomy, the term ToA usually refers to the arrival time of a pulsating signal. In this Thesis, for convenience, the term ToA indicates the arrival time of a single photon.
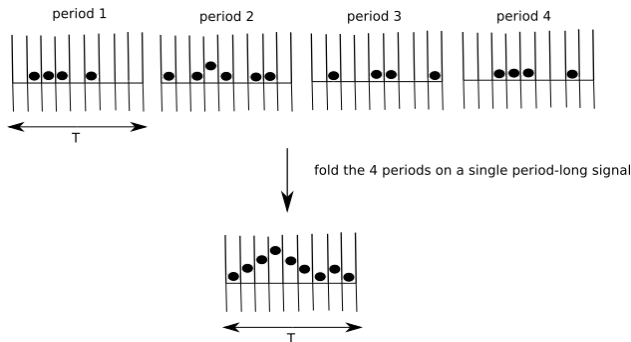
Figure 4.2: Epoch folding, graphical interpretation.

To properly model the phase of a pulsar signal, either the epoch folding is performed at an inertial reference location or the accelerations acting on the photon detector are taken into account. In the first case, the typically used (quasi) inertial reference frame is the International Celestial Reference System (ICRS) whose origin is at the SSB.

4.2 Computation of the Pulsar Phases at SSB and Light Curve Templates

To determine the pulsar phases at SSB, it is necessary first to change the pulsar photons ToAs from the reference frame of the receiver to the ICRS. This procedure is usually named *barycentrization* and is carried out preliminary to the epoch folding (an example of software dedicated to the barycentrization is Tempo2 [40]). In order to perform the barycentrization, the pulsar timing software needs to know the position and the velocity of the time tagging device in the SSB frame. Moreover, for a timing accuracy of about 1 ns it needs to account for relativistic corrections such as Einstein and Shapiro delays. The description for the transformation to convert the measured ToAs to the SSB can be found in [40]. Following the barycentrization process, the pulsar timing properties, like their pulsating periods and drift, can be estimated, e.g. using a χ^2 technique [41].

Once the signal ToAs have been barycentered, the period duration is divided into some equal-length phase bins and, by folding the times over the period, the number of photons in each bin is counted, generating the so called *light curve*. The SNR depends on both the integration time and the number of bins, which are fundamental parameters of the navigation system that have to be decided a priori depending on the required SNR. To have a more precise phase estimation and so a better positioning accuracy, a large number of bins is required. However, the larger the number of bins, the higher the number of photons needed to achieve the desired SNR, which means longer observations or larger telescope areas.

Finally, the *template building* process is performed: an analytical template of the pulsar light-curve can be defined by means of a polynomial fit of the reconstructed light curves (see Chapter 5 for the cases of the Crab, Vela and B0540-69 pulsars). Notice that, in the definition of an analytical template, long observations can be exploited to achieve a high-SNR for the generated light curves, improving the quality of the signal template and hence the performance of the navigation system. The signal template and the estimated timing properties at the SSB can be compared to the phase of the signal reconstructed at the user position for generating a range measurement between the SSB and the user.

4.3   Computation of the Ranging Measurements by the User

The phase of the received pulsar signal changes as the satellite moves along the line-of-sight of that pulsar (Fig. 4.3). Therefore, if the ToAs of the photons in input to the epoch folding are not referred all to the same position and velocity, the phase shift due to the Doppler effect of the spacecraft motion must be removed. Photons ToAs need to be corrected as if they were detected at one particular reference point along the satellite orbit, a task which is referred to as *phase alignment*. This task takes into account both users and

pulsar dynamic effects as well as propagation effects: given the user position and velocity at the reference point, the following measured photons ToAs are referred to the reference point by accounting for the motion of the user (i.e. a dynamic orbit propagation exploiting a precise modeling of the gravitational and non-gravitational forces applied to the satellite), pulsar binary orbital motion, secular motion of the pulsar and solar system dispersion (which in the optical band might be actually negligible). It appears evident that the process for estimating the satellite orbit is an iterative process, where the improvement of the reference point estimation at each iteration improves the phase alignment result and hence the generation of a more precise light curve, leading to a more accurate measurement.
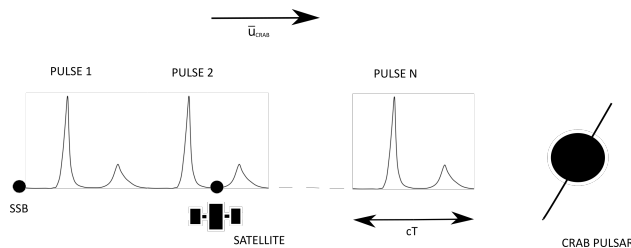
Figure 4.3: Line-of-sight graphical representation for the Crab pulsar.

The aim of a pulsar-based navigation system is to estimate the position and velocity of a satellite starting from the reconstructed pulsar signal. After the phase alignment, folding and binning steps, the reconstructed phase delay measurements of the incoming signal(s) are cross-correlated against the respective signal replica template, which is already available at the user receiver, obtaining the satellite phase estimation $\phi_s(t)$. For what concerns the phase estimation of a periodic signal, different phase estimation techniques have been proposed in the literature. In GNSS, an iterative tracking is typically implemented, where a set of correlators is put on the peak of the cross-correlation function (CCF) between a signal replica and the received signal to mitigate multipath fading effects [43]. In [6] a Maximum-Likelihood Estimator (MLE) has been proposed for pulsar navigation, which directly uses the pulsar photons ToAs for a phase estimation. They showed that

25

the MLE asymptotically achieves the Cramer-Rao Lower Bound (CRLB), but its computational cost is significantly high and not suitable for satellite applications. In [43] a new phase estimation strategy named Fast Maximum-Likelihood (FML) was introduced [44]. In long observations, FML achieves the CRLB with a much smaller computational complexity with respect to MLE. In [42] the proposed phase delay estimator is proven to be more advantageous with respect to the standard CCF maximization approach: it is based on the steepest zero crossing of the phase derivative of the CCF between a template (i.e. the $h(\phi)$ shown in Fig. 1 for the case of the optical profile of the Crab pulsar) and a folded and binned signal. The computational complexity of this method is much smaller with respect to that of the FML and hence it is particularly attractive for satellite applications: the results presented in this Thesis have been obtained through this technique. Fig. 4.4 shows the shape of a cross-correlation function between two template signals of the Crab pulsar along with its phase derivative.
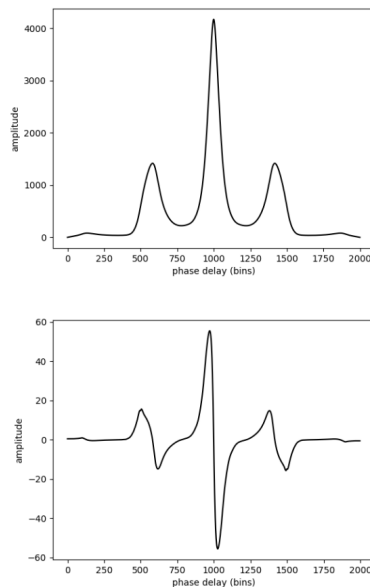

Figure 4.4: Autocorrelation (top) and its phase derivative (bottom) for the Crab pulsar template.

26

From the phase estimate obtained by the cross-correlation, the projection of the baseline between the SSB and the spacecraft is derived. The j-th observed measurement is defined as the difference between the measured time t_j at the user position and that in which the same event reaches the SSB. Letting n_b be the number of phase bins in which the pulsar signal is partitioned into, the measurement is obtained starting from the satellite s phase estimation $\phi_s^k(t_j)$ and the bin size dt (expressed in seconds) as

$$O_j^k = (\phi_s^k(t_j) - \phi^{SSB}(t_j) + i(t_j) \cdot n_b) \cdot dt , \qquad (4.2)$$

where $i(t_j)$ is the counter accounting for the initialization of the integer number of pulses between the satellite and the SSB at the instant t_j, which remains constant until the phase measurement exceeds one cycle, and $\phi^{SSB}(t_j)$ is provided in Equation 3.1. It should be noticed, however, that the term $\phi_s^k(t_j)$ in Equation 4.2 is subjected to both clock errors on board of the satellite and not modeled effects, such as not modeled interstellar medium dispersion and relativistic effects. Since the interstellar medium dispersion scales with a factor of f^{-2}, where f is the frequency of the propagating electromagnetic wave, it is significant only at radio wavelengths. Therefore, the associated computed measurement (i.e. that given by the theoretical model on-board the satellite) is given by

$$C_j^k = \tau_j^k + dt_s(t_j) + \Delta R , \qquad (4.3)$$

where τ_j^k is the light travel time defined in Equation 4.1 computed using the the satellite position known at the satellite, $dt_s(t_j)$ is the total clock error of the spacecraft at the current time instant t_j (referred to a reference epoch t_0) and ΔR accounts for relativistic effects. Notice that a reference frame centered in the SSB has been considered in Equation 4.3 and that the pulsar binary orbital motion and the secular motion of the pulsar - which are assumed to be known - have been accounted for in the phase alignment step. The total clock error $dt_s(t_j)$ can be approximated with a second-order polynomial as [43]

$$dt_s(t) = a_0 + a_1(t - t_0) + a_2(t - t_0)^2 , \qquad (4.4)$$

27

where a_0 is the clock bias (s), a_1 is the clock drift (s/s) and a_2 is the clock aging (s/s^2). The ΔR component is modeled as

$$\Delta R = \Delta E + \Delta S, \tag{4.5}$$

where ΔE and ΔS constitute the so-called Einstein and Shapiro delay respectively, whose expressions are shown in [40].

The final measurements y_j^k from the $k-$th pulsar used for the orbit determination process are

$$y_j^k = c \left(O_j^k - C_j^k \right). \tag{4.6}$$

The y_j^k measurements represent the inaccuracy in the satellite positioning along the line of sight of the k-th pulsar, given by the difference between the measured projected distance from SSB and the nominally computed one. The process is repeated over different subsequent measurement windows (in each of these windows the cross-correlations are performed), where the time delays from the cross-correlation on a variable selectable number of windows can be aggregated and processed by a satellite state vector estimator.

4.4 Computation of the Doppler Measurements by the User

In addition to the range measurement, a Doppler rate measurement can be added to aid the estimator in the orbit determination task. More precisely, a new Doppler measurement is built as a new range measurement is added to the estimator. Therefore, for a single set of photons ToAs, two measurements can be generated. This means that following l pulsar observations, $2 \times l$ measurements are obtained.

The observed Doppler rate measurement referring to the i-th observation window, with $i \in [1, \dots l]$, is built starting from a significance analysis of the light curve. The aim of such an analysis is to estimate the period of the

signal reconstructed starting from a set of ToAs: if the estimated period is lower than the nominal one, the projection of the satellite velocity along the line-of-sight of the pulsar is higher with respect to the one computed on board of the satellite (i.e. the velocity considered for the phase alignment task). Clearly, such an analysis is reliable if the nominal pulsar period known at the spacecraft is known with a high accuracy. For this reason, the pulsar spin-down has to be constantly accounted and a monthly/yearly update of the pulsar ephemerides from a ground segment could be considered. Notice that the knowledge of the pulsar period at the time of investigation is required in any case to carry out the epoch folding step. In the simulations, the significance of a light curve P has been defined as in [7]

$$\chi^2(P) = \sum_{j=1}^{n_b} \frac{(P(j) - \bar{P})^2}{\bar{P}} \qquad (4.7)$$

where $P(j)$ is the number of photons in the j-th phase bin and $\bar{P}$ is the average number of photons in the bins. Equation 4.7 can be exploited to estimate the period of a pulsar signal starting from a set of photons ToAs. The estimated period $\hat{T}$ is the one maximizing Equation 4.7. In other words, if the epoch folding step is carried out with $\hat{T}$, the resulting light curve $\hat{P}$ will maximize the profile significance, i.e.

$$\hat{P} = \arg\max_P \chi^2(P). \qquad (4.8)$$

From the estimated period $\hat{T}$, the projection of the satellite velocity error along the line-of-sight of the pulsar $\mathbf{n}$ can be estimated as

$$\Delta v_n = (\frac{1}{\hat{T}} - \frac{1}{T}) \times c\hat{P} \qquad (4.9)$$

leading to the estimation of the satellite velocity along the line-of-sight of the pulsar (which constitutes the observed measurement)

$$O^D = \hat{v} = \mathbf{v} \cdot \mathbf{n} + \Delta v_n \qquad (4.10)$$

29

where $\mathbf{v}$ represents the velocity known at the satellite i.e. the one used in the phase alignment step. On the other side, the computed Doppler rate measurement is defined as

$$C^D = \mathbf{v} \cdot \mathbf{n}. \tag{4.11}$$

Chapter 5

Simulating Optical Pulsar Signals and Line-of-Sight Positioning Accuracies

5.1   Stochastic Models for Pulsar Signals

Let (t_0, t_f) be an observation time interval. Let t_i be the ToA of the i-th photon and the set $\{t_1, t_2, ...t_M\}$ be a random sequence in increasing order, i.e.

$$t_0 \leq t_1 < t_2 < .... < t_M \leq t_f, \tag{5.1}$$

where M is the number of detected photons in the interval (t_0, t_f). Notice that M is a random variable.

Let $t_0 = 0$ and $N_0 = 0$. Then,

$$N_t = n, t_n \leq t \tag{5.2}$$

is named point process and represents the number of detected photons in the interval $(0, t)$, with t_n the last photon's ToA.

A point process $\{N_t, t > 0\}$ is called a non-homogeneous Poisson process (NHPP) with a time varying rate $\lambda(t) \geq 0$ if it satisfies the following

conditions

1. The probability of detecting one photon in a time interval Δ is given by

$$P(N_{t+\Delta} - N_t = 1) = \lambda(t)\Delta \text{ when } \Delta \to 0 \qquad (5.3)$$

2. The probability of detecting more than one photon in a time interval Δ is given by

$$P(N_{t+\Delta} - N_t \geq 2) = 0 \text{ when } \Delta \to 0 \qquad (5.4)$$

3. Non-overlapping increments are independent where

$$\Delta N = N_t - N_s, \ t > s \qquad (5.5)$$

is the increment of the stochastic process $\{N_t, t > 0\}$.

Fixed a time instant t, the number of detected photons in the interval $(0, t)$, N_t, is a Poisson random variable with parameter

$$\lambda(t) = \int_0^t \lambda(\psi)d\psi \qquad (5.6)$$

that is

$$P(N_t = k) = \frac{(\int_0^t \lambda(\psi)d\psi)^k \exp(-\int_0^t \lambda(\psi)d\psi)}{k!} \qquad (5.7)$$

with mean and variance equal to

$$E[N_t] = \text{var}[N_t] = \int_0^t \lambda(\psi)d\psi \triangleq \Lambda(t). \qquad (5.8)$$

The number of detected photons in any fixed time interval (s, t) comes straightforward from (4.7) i.e. it is a Poisson random variable with parameter

$$\lambda(t) = \int_s^t \lambda(\psi)d\psi \qquad (5.9)$$

that is

$$P(N_t - N_s = k) = \frac{(\int_s^t \lambda(\psi)d\psi)^k \exp(-\int_s^t \lambda(\psi)d\psi)}{k!}.$$ (5.10)

The overall rate function $\lambda(t)$, $t > 0$, represents the aggregate rate of all arriving photons from the pulsar and background i.e.

$$\lambda(t) = \lambda_b + \lambda_s h(\phi_{det}(t))$$ (5.11)

where $h(\phi)$ is the periodic pulsar profile, $\phi_{det}(t)$ the detected phase, and, λ_b and λ_s are the known effective background and source arrival rates respectively [39]. The periodic function $h(\phi)$ is usually defined on the phase interval $\phi \in [0,1)$ (cycle) and can be extended to the entire real line by letting

$$h(\phi + n) = h(\phi),$$ (5.12)

where n is an integer. The function $h(\phi)$ is non-negative and normalized according to

$$\int_0^1 h(\phi)d\phi = 1$$ (5.13)

and

$$\min_\phi h(\phi) = 0.$$ (5.14)

5.2   Pulsar Signals Simulation

The normalized analytical model $h(\phi)$ can be treated as a probability density function to simulate a sequence of pulsating signals. Starting from the pulsar period T ($\simeq 0.0337$ s for the Crab pulsar) and the number of phase bins in

which the pulsar signal phase is partitioned into, one can obtain the photons detection probability for each phase bin as

$$dp(\phi) = \frac{dt}{T}h(\phi) \qquad (5.15)$$

where dt is one-bin length expressed in seconds.

Starting from Equation 5.15 it is possible to simulate a one-period signal detected by an instrument (either a ground or a space telescope) with a given optical configuration. This is possible if the photon fluxes (expressed in photons cm^{-2} s^{-1}) coming from the pulsar (P_C) and from the nebula (N_C) with a given optical configuration are known. In fact, knowing the values of the effective area A_C of the reference telescope (which takes into account the optics reflectivity and the quantum efficiency of the detector) and the FoV F_C of the detector, it is possible to scale the photon flux measured by a satellite instrument with a different effective area A_S and FoV F_S. We assume here that the FoV is sufficiently small to consider the nebula flux uniformly distributed over this FoV. Moreover, assuming the pulsar to be a point-like source, the photon flux of the pulsar will solely depend on the telescope effective area. The photon fluxes measured by the instrument for both the pulsar (P_S) and the nebula (N_S) are thus

$$P_S = P_C \frac{A_C}{A_S} \qquad (5.16)$$

$$N_S = N_C \frac{A_C}{A_S}\frac{F_C}{F_S}. \qquad (5.17)$$

Equation 5.16 can be used to correctly scale the probability function $dp(x)$, leading to a template signal whose entries correspond to the average number of pulsar counts in a specific phase bin. Equation 5.17 instead provides a constant signal, associated to the nebular background. Finally, photon ToAs can be simulated. Assuming a Poisson distribution, the statistic profile corresponds to the average number of detected photons in each phase bin, given by the sum of pulsar and nebula counts. Because of the large

number of pulsar periods received in a second, the photon fluxes in Equation 5.16 and Equation 5.17 are considered to be constant and not dependent on time.

Section (4.3) showed that the phase of the measured pulsar signal can be determined by cross correlating it with a suitable signal template. Clearly, this requires the availability, on board the satellite, of an analytical template for a specific pulsar. The pulse shape is unique for a specific pulsar and usually differs between the radio, optical, X-ray and gamma-ray bands [15]. In this Section the first three optical pulsars in Tab. 1 are considered, i.e. the three optical pulsars with the highest magnitude: B0531+21 (Crab), B0833-45 (Vela) and B0540-69.

In [41] the optical signal coming from the Crab pulsar is described as a summation of sixteen Lorentzian functions of the signal phase ϕ as follows:

$$f_{B0531+21}(\phi) = p \sum_{i=1}^{16} \frac{d_{i-1}{b_i}^2}{{b_i}^2 + (\phi - \phi_1 + h_{i-1})^2} + q \qquad (5.18)$$

where p, q and ϕ_1 are the fitting parameters representing the total signal amplitude, the background level and the phase of the main peak respectively, while ϕ_1, b_i, d_{i-1} and h_{i-1} are numerical coefficients reported in [41].

Fig. 5.1 shows four Crab pulsar simulated light curves. The signals were obtained considering a 1800 s-long observation and a telescope geometric area of 0.07 m^2, varying the telescope field-of-view (706.86 arcsec^2, 78.54 arcsec^2, 19.63 arcsec^2, 0.79 arcsec^2), which correspond to field-of-view diameters of 20 arcsec, 10 arcsec, 5 arcsec, 1 arcsec, respectively. The optics reflectivity and the quantum efficiency of the simulated space instrument are assumed to be those of the reference observatory in Asiago; thus, the photon fluxes are scaled considering the sole geometric areas A_C and A_S. Fig. 5.1 confirms the advantage of a narrow field-of-view, which allows the rejection of a large number of nebular photons. Narrowing the instrument field-of-view allows reduction of the observation time and/or the telescope area improving the

system performance and its optical design.
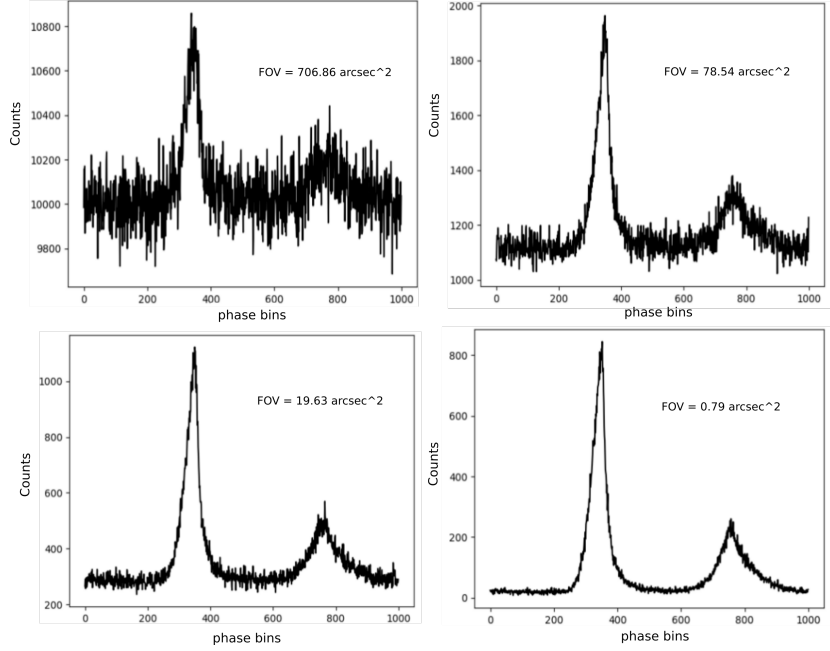
Figure 5.1: Simulating a 1800 s-long observation of the Crab pulsar.

In [45], the analytical template for the optical profile of the Vela pulsar is defined as the summation of six Gaussian functions

$$f_{B0833-45}(\phi) = \sum_{i=1}^{6} k_i \frac{1}{\sqrt{2\pi}\sigma_i} \exp\{-\frac{(\phi - \mu_i)^2}{2\sigma_i^2}\} + C \qquad (5.19)$$

where k_i, σ_i, μ_i and C are reported in [45].

In this Thesis, the analytical expression for the signal replica for the B0540-69 pulsar is defined as the summation of eight sin functions

$$f_{B0540-69}(\phi) = \sum_{i=1}^{8} a_i \sin(g_i\phi + c_i) \qquad (5.20)$$

where a_i, g_i and c_i are the coefficients reported in Tab. 5.1. This template has been obtained starting from the observations reported in [46].

Table 5.1: B0540-69 template parameters.

Parameter	Value	Parameter	Value	Parameter	Value
a_1	1.378	g_1	2.293	c_1	0.4194
a_2	0.4305	g_2	5.256	c_2	2.071
a_3	0.07021	g_3	10.11	c_3	2.791
a_4	0.01741	g_4	17.57	c_4	2.214
a_5	0.007505	g_5	23.14	c_5	2.493
a_6	0.004933	g_6	28.97	c_6	2.686
a_7	0.002408	g_7	35.19	c_7	2.847
a_8	0.001013	g_8	41.04	c_8	2.761

Exploiting the real photon flux measurements reported in [45] and [46] one can simulate optical signals coming from the Vela and from the B0540-69 pulsar. From Fig. 5.2 and Fig. 5.3 it can be seen that the Vela and the B0540-69 pulsars are characterized by weaker photon fluxes with respect to that of the Crab pulsar. This means that longer observations are required to achieve the same SNR with a given optical configuration. Fig. 5.2 and Fig. 5.3 show the result of the cross-correlation between the pulsar analytical template and a reconstructed signal for the Vela and the B0540-69 pulsars.

5.3 Line-of-sight Positioning Accuracies

Comparing the simulated signal measurable on a satellite with the nominal one, it is possible to estimate the positioning accuracy of the satellite along the line-of-sight of a specific pulsar. Generating a large number of signals, it can be shown that a Gaussian distribution with zero-mean and variance σ^2

observation time =7200 s
telescope area = 0.07 m^2
field-of-view = 0.79 arcsec^2

Vela template
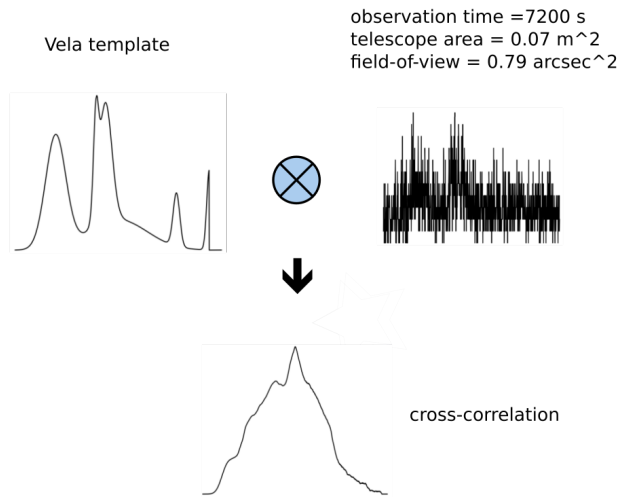
cross-correlation

Figure 5.2: Cross-correlation example for the optical Vela pulsar signal.

observation time =7200 s
telescope area = 0.07 m^2
field-of-view = 0.79 arcsec^2

B0540-69 template
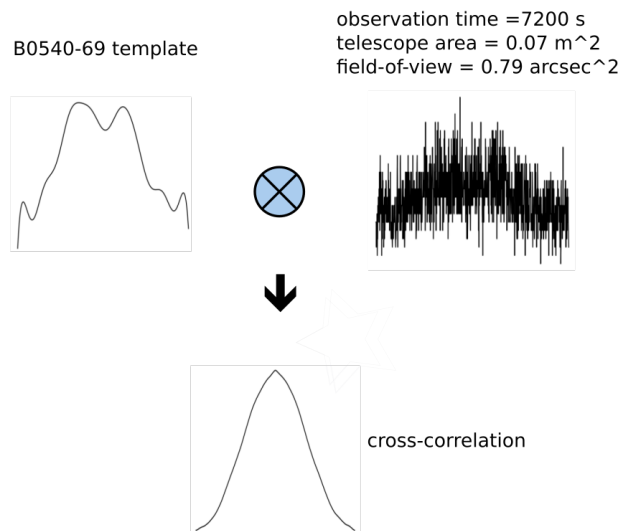
cross-correlation

Figure 5.3: Cross-correlation example for the optical B0540-69 pulsar signal.

well-approximates the phase measurement errors, defined as the difference between the imposed and the estimated phase shifts. Tab. 5.2 reports the value of σ, i.e. the positioning accuracy along the line-of-sight of a pulsar, obtained with a telescope area of 0.07 m^2 over a field-of-view of 0.79 arcsec^2. The results have been obtained using the phase delay estimation technique (based on the search of the steepest zero crossing of the derivative of the cross-correlation function between the signal replica and the simulated signal) described in Section 4.

Table 5.2: Positioning error along the line of sight of the Crab pulsar attainable with a telescope area of 0.07 m^2 over a field-of-view of 0.79 arcsec^2.

Integration	Accuracy (m)		
Time (s)	Crab	Vela	B0540-69
10	13942	5626222	1698983
100	6465	2062948	444466
500	2222	1176148	93292
1000	1818	297386	48087
2000	1414	184861	25636
4000	707	123241	21237
8000	404	21433	15169

The behaviour of the line-of-sight positioning error with different effective areas and fields-of-view can be investigated, and the Crab pulsar has been considered for the analysis. Fig. 5.4 displays the logarithm of σ (expressed in seconds, i.e. dividing it by the speed of light) as a function of the observation time, obtained with a telescope with a geometric area of 0.07 m^2 with different values of FoV dividing the pulsar period in 1000 bins. The results are equally

spaced, on the observation time axis, for a better representation. The results show the advantages of a narrow FoV, which allows the rejection of a large number of photons from the nebula, increasing the SNR. Fig. 5.5 considers a telescope with an area of 0.2 m^2 (i.e. about 50 cm diameter), with the same FoV values considered in Fig. 5.4: it is evident that the larger the telescope and the smaller the FoV, the better the attainable timing accuracy.

It can be clearly seen that σ decreases faster with a larger effective area and a narrower FoV. With larger values of FoV, σ decreases slowly and longer observation times are needed to decrease the line-of-sight positioning error. The decrease of σ becomes slower as the observation time increases, hence making the improvement in the PAT estimation accuracy not significant for long observation times, especially if the FoV is larger. For this reason it may be not convenient, in a SNOP system, to choose too long observation times. Actually, this analysis shows that it could be more convenient to choose shorter observation times and reconstruct a larger number of signals to fit the satellite state parameters along its orbit.
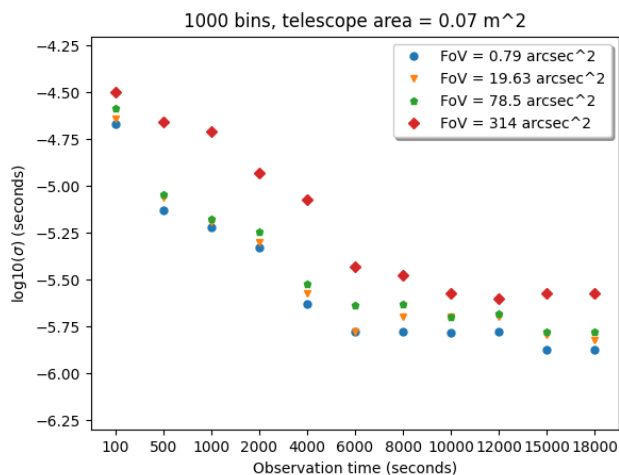

Figure 5.4: Crab pulsar: σ with an 0.07 m^2 area optical telescope, 1000 bins case.

An analysis of this type allows also to understand whether it is conve-
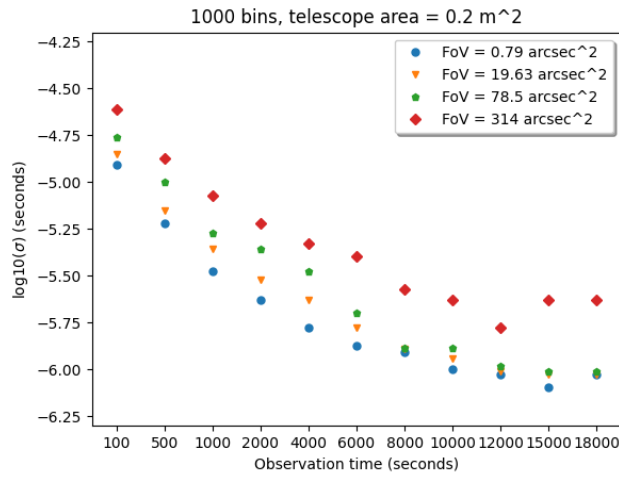
Figure 5.5: Crab pulsar: σ with an 0.2 m^2 area optical telescope, 1000 bins case.
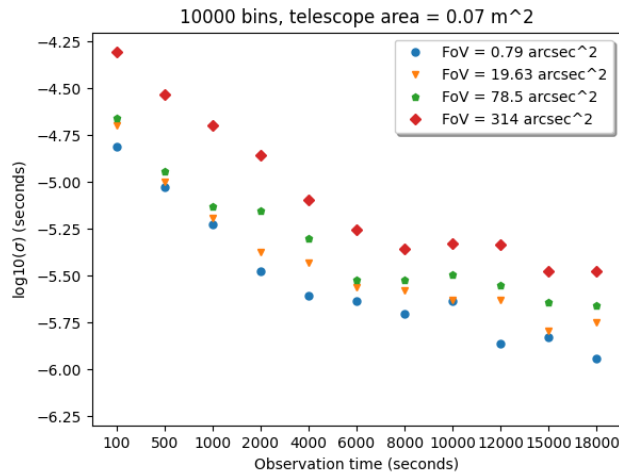
Figure 5.6: Crab pulsar: σ with an 0.07 m^2 area optical telescope, 10000 bins case.
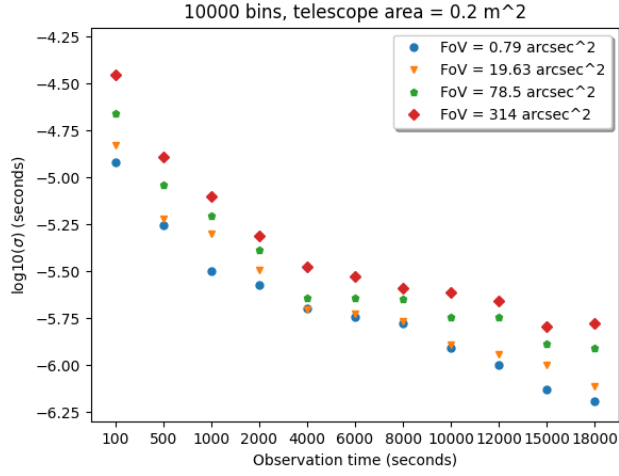
Figure 5.7: Crab pulsar: σ with an 0.2 m^2 area optical telescope, 10000 bins case.

nient to increase the binning density or not (see Fig. 5.6 and Fig. 5.7). For instance, up to 8000 s of observation, increasing the number of phase bins from 1000 to 10000 does not improve the PAT estimation accuracy with a telescope area of 0.07 m^2 over a FoV of 0.79 arcsec^2 (Fig. 5.4 and Fig. 5.6). Therefore, for observation times shorter than a certain threshold T_s, a lower binning resolution is suggested. This threshold has to be computed case-by-case, taking into account the instrument design parameters. In the reported case (geometric area = 0.07 m^2 and FoV = 0.79 arcsec^2), $T_s \approx 8000$ s. Increasing the length of the observation above T_s, the higher binning resolution will provide a more accurate PAT estimation than the lower binning resolution.

Chapter 6

Satellite State Estimation Based on Optical Pulsar Measurements

The way the system exploits the pulsar signal(s) for navigation is by minimizing the phase differences between the reconstructed signal(s) and the signal template(s) at the SSB. A filtering system with orbital dynamic modeling (e.g. batch least-squares, sequential Kalman filter, sequential batch filter) is then exploited to estimate the satellite orbit and clock error parameters over the reconstructed signal phase.

6.1 Navigation Filter Initialization Technique

The preferred approach to initialize the pulsar navigation filter would be from a priori information available on board, for example the propagation of a position determined during the early stage of the mission. The navigation filter initialization could be aided also by other autonomous technologies such as those presented in [13] and [14], if available. If an a priori information about the position is not available, either because of instrument malfunctioning or other reasons, the only way to initialize the pulsar navigation filter based on the sole pulsar signals is by observing three (four, if the satellite clock error must also be initialized) or more pulsars. It should be noticed, however, that

the integer number of pulses between the pulsar and the satellite is unknown (ambiguity problem, [10]). Therefore, an error up to the space traveled by the signal in one pulsar period (e.g. about 10000 km for the Crab) would be tolerable in the filter state vector initialization. By observing different pulsars the ambiguity problem can be constrained or solved [5].

If $N > 1$ pulsars are needed to be observed, it could be done either simultaneously (with N different detectors) or sequentially (with a single detector). The former choice would unavoidably result in an increasing technical complexity of the navigation payload, but would allow a faster update rate of the navigation parameters, hence increasing the system reliability. The latter choice would drastically reduce the system weight and cost, at the expense of a poorer-performing system and the need for reorienting the telescope and/or the satellite toward the desired pulsating source. However, when the satellite has initial information on its position, the computation and operation complexity can be reduced and a single pulsar would be sufficient to determine the satellite orbit.

6.2   The Sequential-Batch Estimation

Assuming that the filter has been initialized and that the ambiguity $i(t_j)$ has been determined as described in Section 6.1 (and hence it is not necessary to account for $i(t_j)$ in the state vector), the orbit determination and time synchronization are obtained by means of an algorithm based on sequential batch filtering. The state vector consists of the satellite position and velocity and the receiver clock bias and drift. The estimate of the state vector at epoch t_{j-1}, $\hat{\mathbf{x}}_{j-1}$ (with the symbol $\hat{\ }$ denoting the estimation), can be propagated in time by the relation

$$\bar{\mathbf{x}}_j = \mathbf{\Phi}_{j,j-1}\hat{\mathbf{x}}_{j-1}\,, \tag{6.1}$$

where $\bar{\mathbf{x}}_j$ is the predicted state at epoch t_j (with the symbol $\bar{\ }$ denoting the prediction) and $\mathbf{\Phi}_{j,j-1}$ denotes the state transition matrix from epoch t_{j-1} to

t_j, and the associated predicted state vector covariance matrix is given by

$$\overline{\mathbf{P}}_j = \mathbf{\Phi}_{j,j-1}\mathbf{P_{j-1}}\mathbf{\Phi}_{j,j-1}^{\mathsf{T}} + \mathbf{\Gamma}_{j,j-1}\mathbf{Q}_{j-1}\mathbf{\Gamma}_{j,j-1}^{\mathsf{T}}, \tag{6.2}$$

where $\overline{P}_j$ is the predicted state covariance matrix at epoch t_j, $\Gamma_{j,j-1}$ is the process noise transition matrix, and Q_{j-1} (positive semi-definite $\forall\, j$) is the process noise covariance matrix.

Assuming that n measurements have been obtained from m pulsars (with $m \geq 1$) over as many observation windows, each of duration T_m, and calling this set of measurement a *segment*, the state deviation vector $d\mathbf{x}_0$ from an a priori propagation $\bar{\mathbf{x}}_0$ with associated error covariance matrix $\bar{P}_0$ at the reference epoch t_0 is estimated. The state vector and its covariance matrix of each segment can be initialized using Equation 6.1 and Equation 6.2 starting from the estimation obtained for the previous segment (except that for the first segment, whose initialization is described in Section 6.1). The reference position is selected in such a way that it lies in the middle of the segment, for minimizing the border effects of the estimation. Notice that $\bar{\mathbf{x}}_0$ is used to initialize the computed measurements defined in Equation 4.3.

The state vector contains eight elements (but it could also contain further parameters linked to force models of the satellite, e.g. solar radiation pressure coefficients) referred to the segment reference epoch t_0 and it is given as

$$\mathbf{x}_0 = \left[\mathbf{r}_{s0}^{\mathsf{T}}, \mathbf{v}_{s0}^{\mathsf{T}}, \mathbf{a}_{s0}^{\mathsf{T}}\right]^{\mathsf{T}}, \tag{6.3}$$

where $\mathbf{r}_{s0}$ denotes the 3D satellite position vector in a SSB reference frame, $\mathbf{v}_{s0}$ denotes the 3D satellite velocity and $\mathbf{a}_{s0} = [a_0, a_1]$. Depending on the time window length and the clock accuracy, it can be the case that just the clock bias a_0 and drift a_1 should be fitted, which is the case assumed in this Section.

The n measurements y_j^k are described by the observation state equations

$$y_j^k = \tilde{H}_j^k d\mathbf{x}_0 + \epsilon_j^k, \; j = 1, \ldots, n, \tag{6.4}$$

where ϵ_j^k is the measurement noise, assumed to be zero-mean and with variance σ_j^k, $\tilde{H}_j^k$ is the observation-state mapping matrix given by

$$\tilde{H}_j^k = \frac{\partial G^k(\mathbf{x}, j)}{\partial \mathbf{x}} \tag{6.5}$$

and $G^k(\mathbf{x}, j)$ are the observation-state relationship evaluated on the reference trajectory. The relation between the measurements y_j^k and the state deviation vector $d\mathbf{x}_0$ is expressed as

$$\mathbf{y} = H d\mathbf{x}_0 + \epsilon = \begin{bmatrix} H^{1\mathsf{T}} \dots H^{m\mathsf{T}} \end{bmatrix} d\mathbf{x}_0 + \begin{bmatrix} \epsilon^{1\mathsf{T}} \dots \epsilon^{m\mathsf{T}} \end{bmatrix} \tag{6.6}$$

where $\mathbf{y} = [y_1^1, \dots, y_n^1, \dots, y_1^m, \dots, y_n^m]^\mathsf{T}$, H denotes the measurements matrix, each H^k is its sub-matrix for the pulsar k, for $k = 1, \dots, m$, ϵ denotes the measurement noise, assumed to be zero-mean and with covariance matrix Σ and $\epsilon^k = \begin{bmatrix} \epsilon_1^k, \dots, \epsilon_n^k \end{bmatrix}^\mathsf{T}$ the measurement noise for the $k-$th pulsar with covariance matrix $\Sigma^k = \bigoplus_{j=1}^n \sigma_j^k$, being $\bigoplus$ the direct sum of matrices.

The state deviation vector estimation, $\hat{d}\mathbf{x}_0$, can be computed using a batch processor, whose normal equation form yields

$$\left(H^\mathsf{T} \Sigma^{-1} H + \bar{P}_0 \right) \hat{d}\mathbf{x}_0 = H^\mathsf{T} \Sigma^{-1} \mathbf{y} + \bar{P}_0 \bar{d}\mathbf{x}_0. \tag{6.7}$$

Defining

$$H^\mathsf{T} \Sigma^{-1} H + \bar{P}_0 = \Lambda = \begin{bmatrix} \Lambda^{1\mathsf{T}} L^1 \dots \Lambda^{m\mathsf{T}} L^m \end{bmatrix}^\mathsf{T} \tag{6.8}$$

and

$$H^\mathsf{T} \Sigma^{-1} \mathbf{y} + \bar{P}_0 \bar{d}\mathbf{x}_0 = N = \begin{bmatrix} N^{1\mathsf{T}} L^1 \dots N^{m\mathsf{T}} L^m \end{bmatrix}^\mathsf{T}, \tag{6.9}$$

the matrices Λ^k and N^k can be accumulated over the segment as (assuming the measurements to be uncorrelated in time)

$$\Lambda^k = \bar{P}_0 + H^{k\mathsf{T}} \Sigma^{-1} H^k = \bar{P}_0 + \sum_{j=1}^n \left[\tilde{H}_j^k \boldsymbol{\Phi}_{j,j-1} \right]^\mathsf{T} \Sigma_j^{k-1} \tilde{H}_j^k \boldsymbol{\Phi}_{j,j-1} \tag{6.10}$$

and

$$N^k = \bar{P}_0 \bar{d}\mathbf{x}_0 + H^{k\mathsf{T}} \Sigma^{k-1} \mathbf{y} = \bar{P}_0 \bar{d}\mathbf{x}_0 + \sum_{j=1}^n \left[\tilde{H}_j^k \boldsymbol{\Phi}_{j,j-1} \right]^\mathsf{T} \Sigma_j^{k-1} \mathbf{y}^k. \tag{6.11}$$

The linear unbiased minimum variance estimate of $d\mathbf{x}_0$ is given as solution of the normal equation

$$\hat{d\mathbf{x}}_0 = \Lambda^{-1} N \, . \tag{6.12}$$

Generally, the normal equation would not be solved by a direct inversion of the information matrix Λ^{-1} but rather by a more accurate technique, such as a Cholesky decomposition. Because of the required linearization to be applied to the system, Equation 6.7 is iterated to convergence until $\hat{d\mathbf{x}}_0$ does not change significantly anymore. At each iteration i, the initial condition $\hat{\mathbf{x}}_0$ is augmented by the value of $\hat{d\mathbf{x}}_0$, that is

$$\hat{\mathbf{x}}_{0_i} = \hat{\mathbf{x}}_{0_{i-1}} + \hat{d\mathbf{x}}_{0_i} \, , \tag{6.13}$$

so that, after the last iteration, the initial state vector $\hat{\mathbf{x}}_0$ represents the best knowledge of the initial position, velocity and clock error values at the reference epoch.

After convergence of the least square iterations, the phase alignment, folding, binning, correlation and batch solution must be repeated, until the satellite phase estimation $\phi_s^k(t_j)$ and its state vector estimation $\hat{\mathbf{x}}_0$ do not change significantly anymore. This whole process is then repeated: after other n measurements are performed, a new segment is created and the state vector is propagated at the reference epoch of this new segment.

6.3 Satellite Clock Error Estimation with Known Position and Velocity

The period stability values of the optical sources in Tab. 3.1 are stable enough for providing a clock reference for the navigation system. In case position and velocity of the spacecraft are known, for example because they are estimated with other techniques from ground, the optical pulsar measurements can be used to synchronize the satellite clock reference to the pulsar time scale. In this case it is sufficient to obtain measurements from a single pulsar. The

sequential-batch filter described in Section 6 can still be adopted, with the state vector that is simplified as $\mathbf{x} = \mathbf{a}$. Alternatively, a pure sequential filter (e.g. an Extended Kalman Filter) can be implemented by defining the state vector as $\mathbf{x} = dt_s(t_j)$ and, subsequently, fitting the a_0, a_1 and a_2 clock parameters over the estimated dt_s clock errors included in a time window of l epochs, from t_{j-1} to t_{j-l-1}. The fit result is defined as $\hat{\mathbf{a}} = [\hat{a}_0, \hat{a}_1, \hat{a}_2]^\mathsf{T}$ and their covariance matrix as $\mathbf{P}_{\hat{\mathbf{a}}}$. The clock parameters are not estimated directly as part of the state vector to avoid the correlation among them which would degrade the sequential filter solution. Assuming the clock parameters to be constant in time, they can be used to propagate the clock state to the next epoch with a state transition matrix defined as

$$\mathbf{\Phi}_{j,j-1} = \begin{bmatrix} 1 & \Delta t_j & \Delta t_j^2 \end{bmatrix}, \tag{6.14}$$

where Δt_j is the time interval between consecutive observations, assumed to be constant. Thus, the predicted state system is

$$\bar{\mathbf{x}}_j = \mathbf{\Phi}_{j,j-1}\hat{\mathbf{x}}_{j-1} \tag{6.15}$$

and the associated predicted state vector covariance matrix is given by

$$\bar{\mathbf{P}}_j = \mathbf{\Phi}_{j,j-1}\mathbf{P}_{\hat{\mathbf{a}}}\mathbf{\Phi}_{j,j-1}^\mathsf{T} + \mathbf{\Gamma}_{j,j-1}\mathbf{Q}_{j-1}\mathbf{\Gamma}_{j,j-1}^\mathsf{T}, \tag{6.16}$$

where $\mathbf{\Gamma}_{j,j-1}$ is the process noise transition matrix and $\mathbf{Q}_{j-1}$ is the process noise.

The measurement vector $\mathbf{y}_j$ is the phase delay between the barycentered signal and the template at the SSB while the design matrix $\mathbf{H}_j$ can be defined as

$$\mathbf{H}_j = \mathbf{e}_N, \tag{6.17}$$

where $\mathbf{e}_N$ is an all-ones vector of length N. The measurement residual $\widetilde{\mathbf{y}}$ and its covariance matrix become respectively

$$\widetilde{\mathbf{y}}_j = \mathbf{y}_j - \mathbf{H}_j\hat{\mathbf{x}}_j, \tag{6.18}$$

$$\mathbf{S}_j = \mathbf{H}_j\bar{\mathbf{P}}_j\mathbf{H}_j^\mathsf{T} + \mathbf{R}_j, \tag{6.19}$$

where $\mathbf{R}_j$ is the measurement noise. The optimal Kalman gain $\mathbf{K}_j$ is computed as

$$\mathbf{K}_j = \bar{\mathbf{P}}_j \mathbf{H}_j^\mathsf{T} \mathbf{S}_j^{-1} \,, \tag{6.20}$$

leading to the determination of the updated state $\hat{\mathbf{x}}_j$ and its covariance matrix $\hat{\mathbf{P}}_j$ as

$$\hat{\mathbf{x}}_j = \bar{\mathbf{x}}_j + \mathbf{K}_j \widetilde{\mathbf{y}}_j \,, \tag{6.21}$$

$$\hat{\mathbf{P}}_j = (\mathbf{I} - \mathbf{K}_j \mathbf{H}_j) \, \bar{\mathbf{P}}_j \, (\mathbf{I} - \mathbf{K}_j \mathbf{H}_j)^\mathsf{T} + \mathbf{K}_j \mathbf{R}_j \mathbf{K}_j^\mathsf{T}. \tag{6.22}$$

The Kalman filter described in this section can be used, for example, in combination with the sequential-batch approach described in Section 6.2, given that the batch filter provides a higher robustness for estimating the orbit against the very noisy range measurements of the pulsar. The estimation of the onboard reference oscillator error (whose propagation precision degrades typically faster than the one of the orbit for non-atomic oscillators) can still be updated more frequently with the Kalman filter, using a numerical propagation of the latest orbit estimated by the sequential batch filter as known positions and velocities of the satellite in input to the filter.

6.4 Satellite State Estimation: a Two-stage Strategy

The statistical dependence between the clock error parameters and the satellite position and velocity reflects in a rank defect in the least squares system. In a single-pulsar scenario, all of the pulsar measurements come from a single direction, making the simultaneous estimation of the eight parameters not possible. Notice that the pulsar directions are practically constant in the whole solar system, leading to a set of measurements from directions which do not change over the time. Also introducing measurements from the other two brightest optical sources, i.e. the the Vela and the PSRB0540-69 pulsars, does not solve the problem. In fact, at least four pulsars would be required to estimate the eight parameters simultaneously, hence arising the need of

an alternative strategy also in a three-pulsar case, although a multi-epoch approach is considered.

To overcome this limit, a two-stage estimation strategy is proposed. In the first stage, the satellite collects l measurements and estimates the clock error parameters only with the sequential batch filter proposed in Section 6.2. Once the clock bias and drift have been estimated, the satellite is responsible for correcting the photons' ToAs to compensate for the clock error contribution. Then, in the second stage, the corrected ToAs are exploited to construct the l measurements for determining the satellite orbit.

Chapter 7

Optical Design of the Navigation Payload

The optical payload for a SNOP system can be divided into three subsystems: the Optical Head (OH), the Pointing System (PS), and the System Electronics (SE), which includes the software. The OH consists of a very narrow field-of-view optical telescope, which focuses the radiation from the selected pulsars on an ultra-fast photon-counting detector; in addition, because of the narrow field-of-view, the telescope has to be coupled to a co-aligned Context Camera (CC), which is also part of the OH. The OH has to be mounted on a PS on-board the spacecraft, to allow the telescope fine pointing independently of the spacecraft orientation. The PS has to interface with the CC, whose stellar map has to be properly analysed by the SE to provide the necessary pointing information. The output signals by the photon counting detectors will have to be time-tagged by the SE, which is synchronized with the on-board clock, so providing the photon ToAs. The ToAs have then to be properly reduced by a suitable software to provide the required information on the spacecraft position in the solar system.

7.1 The Optical Head

The OH subsystem, shown in Fig. 7.1, is composed by three main elements: the Optical Telescope (OT), the Pulsar Camera (PC) and the CC. The OT is responsible for collecting the incoming photons and for directing them to the two channels of the PC and the CC. The choice of a double-channel optical system comes from the need of both time tagging the pulsar photons collected over a FoV (to limit the pulsar background noise) and providing larger FoV images to track the optical source, pointing the OT to the correct direction by means of the PS. The two tasks are performed by the PC and the CC respectively. An accurate description for the OT is provided in [47].

The light beam coming from the OT is split into the two channels by means of a folding mirror with a small central hole. The light passing through the hole is directed to the PC channel while that reflected by the folding mirror goes to the CC channel. The central hole is responsible for limiting the source background noise leading to a higher SNR of the reconstructed signal thus increasing the accuracy of the navigation system.

Because of the need of the folding mirror, the telescope focus has to be placed behind the telescope itself. To limit the instrument size and to minimize mechanical and structural issues, another folding mirror is placed along the optical path of the PC channel. Thus, both channels lie in the same direction. To enhance the compactness of the system, a suitable lens system can be considered in the design of the two cameras reducing their focal lengths. Examples of such systems are the Cooke triplet, the Petzval objective and the Petzval derivative.

A telescope diameter of 0.3 m has been deemed suitable for the navigation payload. A Ritchey-Chretien configuration (i.e. an optical telescope with two hyperbolic mirrors) with a focal length of 700 mm has been adopted. Since a Ritchey-Chretien telescope is usually characterized by a narrow field-of-view (a few arcminutes), a split doublet (i.e. two positive lenses) has been added to reach the field-of-view specified for the CC. The split doublet is added in

such a way the two lenses and their mechanical support are integrated into the primary mirror of the OT.

The light beam coming from the OT is split into the two channels by means of a folding mirror with a small central hole, with a diameter equal to 1 mm. The light passing through the hole is directed to the PC channel, whose circular field-of-view is of 19.63 arcsec^2. The light is then re-focalized after the telescope focus by means of a double lens system, for a total focal length of 2062.7 mm. A 50 μm diameter photon counting detector is assumed in the optical design.

On the other side, the light reflected by the folding mirror goes to the CC channel. The field-of-view of the CC is of $1° \times 1°$, with a 10 mm square size detector. To adjust the focal length of the CC, a Cooke triplet with a 190 μm out-of-focus focal plane has been selected.

The detector of the PC is a Single Photon Avalanche Diode (SPAD), or a small SPAD array, for redundancy. This type of sensor produces a very fast electrical pulse at each photon detection. These pulses can then be properly shaped by a suitable fast electronics and give an optical output to be sent to the SE. This optical signal will allow to define the ToA to be associated to each detected photon. The detector of the CC will be a common CMOS APS sensor. A detector like FaintStar [50] has been deemed suitable for the system. FaintStar is a one megapixel image sensor with 10 μm pixels and rolling shutter. The chip has pixels-to-centroids processing, including transfer curve linearization, bad pixel replacement, background image estimation and suppression, spike filtering, bright object extraction, and photometric barycentre calculation. This would allow to transfer to the SE only the centroids coordinates, so reducing the data rate to the SE.

7.2   The Pointing System

Regarding the study of a pointing system, two different errors need to be considered: pointing errors and knowledge errors. The former represent the
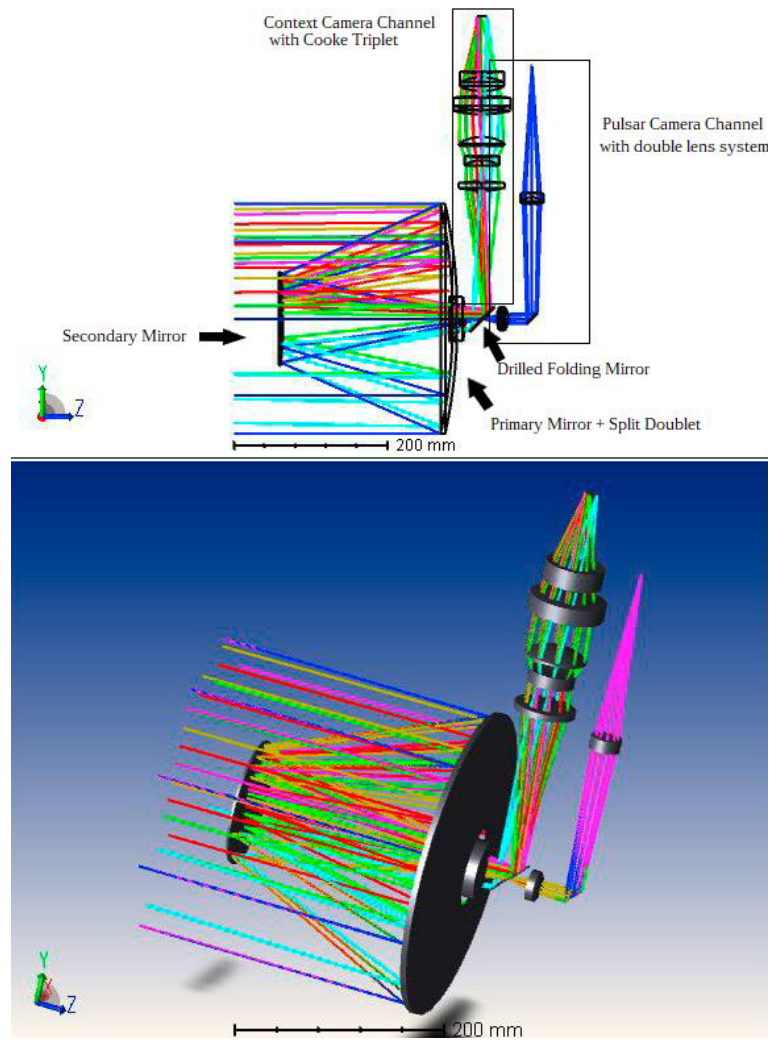
Figure 7.1: 2D and 3D representations of the optical payload.

effective pointing errors of the system during the target observation, while the latter represent the difference between the actual pointing and the one known - in a given reference frame - at the spacecraft and can be both further partitioned into their absolute, mean and rate components. A SNOP system imposes quite demanding pointing accuracies for observations lasting even several hours. Nevertheless, present technologies allow to reach a mean pointing error of less than 0.1 arcsec, hence confirming the feasibility of the narrow pointing required by a SNOP system. On the other hand, an absolute knowledge error of about $0.5°$ is usually reached on a spacecraft after its launch, which can be then highly reduced by means of in-flight calibrations. Considering the $1°\times1°$ field-of-view of the CC, such a knowledge error has been deemed suitable for the system. Examples of pointing systems achieving a sub-arcsec pointing accuracy can be found in both complex spacecraft and small satellites (e.g. Cubesats). Two examples are the Fine Guidance Sensor on-board of Euclid [48] and the pointing system on-board of CubeSpec [49].

As described in the previous subsection, the system OH has to be able to point the observed target and to track it for the necessary integration time; for this, it is necessary to mount the OH on a suitable pointing system structure. Since the requirement is to maintain the target within a field-of-view of the order of a few arcseconds, it will be necessary to mount the OH on an accurate two-axis rotation stage. The range of rotation will need to be rather large, to allow the OH to point at the target minimizing the spacecraft rolls. At the same time, it will be necessary to point at the target with high accuracy. For this, several mechanical solutions are possible, but it could be envisaged to use coarse/fine rotation stages: the first to quickly arrive at the pointing region, the second for the fine pointing.

The control of the PS will be dual: for the coarse positioning, information from the spacecraft attitude will have to be provided to the SE that will transform it in a rotation to bring the OH in the pointing region. For the fine pointing, the SE will compare the acquired CC field stellar map with an on-board one to define the final fine rotation needed to bring the observable

target within the narrow PC field-of-view. For the whole duration of the acquisition time, it will be necessary to periodically acquire a stellar map with the CC to check the actual system pointing.

7.3 The System Electronics

The SE will have to accomplish several tasks.

- Interfacing with the PS to command/control the OH pointing.

- Interfacing with the OH to collect the photon pulses from the PC and the background view from the CC.

- Performing data reduction:

    - the photon pulses will be converted in photon ToAs by a suitable Time to Digital Converter (TDC) synchronous with the on-board clock and stored in a mass memory; at the end of the acquisition, the stored ToAs will be properly reduced to generate the pulsar light curve, from which it will be possible to derive the navigation data;

    - the background view acquired by the CC will be correlated with the on-board stellar map of the same observed sky portion to define the optimal pointing of the OH; these data will be used by SE to command and control the PS;

- Interfacing with the spacecraft: in addition to House Keeping data, this interface is necessary to provide to the SE the information about the S/C pointing, the reference clock (to discipline the electronics and properly time tag the detected photons) and to exchange the navigation data.

Chapter 8

PODS: a Pulsar-based Orbit Determination Software

The aim of this Chapter is to introduce Pulsar-based Orbit Determination Software (PODS), a novel simulation environment developed to test the performance of a pulsar-based navigation system. The software is intended for systems making use of photon-counting instruments such as optical, X-ray and gamma-ray detectors. PODS is fully written in Python and is an Orekit-based software [51].

8.1 Software Description

One of the key advantages of PODS is its capability of easily simulating a wide set of orbits in the solar system, as described in [51]. The orbit definition is made either via the propagation of an initial position-velocity (PV) state or through the description of the six Keplerian parameters (i.e. semimajor-axis, eccentricity, inclination, right ascension of the ascending node, perigee argument and mean/true anomaly). PODS allows also to easily add external forces such as solar radiation pressure, third body perturbations, atmospheric drag and relativistic effects since it is based on Orekit, providing a realistic estimation of the system performance.

Once the orbit has been defined, a numerical propagator is built to propagate the satellite state at a specific date of interest, by means of a Dormand Prince 853 variable step-size orbit integrator. The step size of the integrator is reduced as the satellite velocity increases. The minimum and the maximum values for the step-size can be chosen by the user depending on the specific simulation requirements.

Two orbits are created in PODS: the true orbit and the guess orbit. The first is the orbit used for the generation of the photons ToAs; the second is the orbit which is known at the satellite, usually different from the former because of the errors in the orbit determination performed on board of the satellite. The force models considered for the ToAs generation differ from the ones exploited for the orbit determination task. More precisely, simpler models have been chosen for the orbit determination, leading to a more realistic scenario. Along with the two orbits, PODS requires the user to specify the pulsars to be observed asking for their International Celestial Reference Frame (ICRF) coordinates. The unit vector describing the pulsar direction in ICRF coordinates is used to compute the advancement of the satellite along the line-of-sight of the pulsar, allowing to determine the phase of a pulsed signal at the current satellite position. To date, PODS provides the user with the analytical templates for the optical signals from the Crab, Vela and B0540-69 pulsars.

PODS considers a reference frame (ICRF) which is centred at the SSB, a point in which the pulsar signal phase can be considered to be known. Then, the phase $\phi_s(t)$ of the pulsar signal at the satellite can be computed starting from that at the SSB $\phi_{SSB}(t)$ (expressed in phase bins) as

$$\phi_s(t) = \phi_{SSB}(t) + \frac{\frac{([x_s(t), y_s(t), z_s(t)] \cdot \mathbf{n})}{c}}{dt} \ , \tag{8.1}$$

where $[x_s(t), y_s(t), z_s(t)]$ is the vector defining the satellite position at the time instant t, $\mathbf{n}$ is the unit vector defining the pulsar direction, dt is the bin size expressed in seconds, c is the speed of light and the $\cdot$ indicates the scalar product. Notice that the signal phase is defined on the interval $[0,1)$

leading to a circular shift of a signal whose phase corresponds to $\phi_{SSB}(t)$. The software is optimized to account for rounding errors (for example, a phase shift of 1.2 bins has the same effect of a phase shift of 1.0 bins) in the circular shift of the phase.

In PODS, the observation of different pulsars can be both subsequent or simultaneous. In the former case, the telescope area and the field-of-view remain fixed since a single-telescope system is assumed; in the latter case, PODS assumes the number of telescopes to be that of the number of observed sources and hence different optical configurations can be adopted. Tab. 8.1 shows a test example for the simultaneous observations case.

Table 8.1: Simultaneous observations example.

Observed source	Date (TDB)		Observation Time (s)	Telescope Area (m^2)	Field-of-View (arcsec^2)	Number of Bins
PSR B0531+21	Nov 8,	2025	4044	0.07	0.79	1000
	23:22:07.1					
PSR B0540-69	Nov 8,	2025	8088	0.2	0.79	500
	23:22:07.1					
PSR B0833-45	Nov 8,	2025	12132	0.2	0.79	500
	23:22:07.1					
PSR B0531+21	Nov 9,	2025	4044	0.07	0.79	1000
	00:06:07.1					
PSR B0531+21	Nov 9,	2025	4044	0.07	0.79	1000
	00:50:07.1					
PSR B0540-69	Nov 9,	2025	8088	0.2	0.79	500
	00:50:07.1					

The orbit determination filter consists in a sequential batch least-squares filter and the Orekit's validated one was exploited. The filter takes in input the collected measurements (whose number and the length of the observations can be defined by the user) and returns a propagator configured with estimated orbits as initial states (i.e. the satellite position and velocity at the middle of the segment) and the other estimated parameters (i.e. the clock error bias and drift). This is done with the aid of a Levenberg-Marquardt optimizer and is iterated leading to the collection of other measurements to re-update the guess orbit and the clock error parameters. By default, the parameters of the Levenberg-Marquardt optimizer are chosen as follows:

1. initial step bound factor = 100

2. cost relative tolerance = 1e-10

3. parameters relative tolerance = 1e-10

4. orthogonality tolerance = 1e-10

8.2   The Ambiguity Problem in PODS

In PODS the ambiguity problem is accounted by defining a floating point variable, hereafter referred to as ambiguity index. The ambiguity index defines the number of pulses between the satellite and the SSB such that it is positive if the satellite position lies between the pulsar and the SSB along the line-of-sight of the pulsar, while it is negative if the SSB lies between the satellite and the pulsar. The number of ambiguity indexes corresponds to the number of selected pulsars. Clearly, the initialization of the ambiguity indexes is made considering the orbit which is known at the satellite i.e. the guess orbit. As the satellite moves along the line-of-sight of a pulsar, the relative ambiguity index is updated as

$$i(t) = i(t - t_0) - \delta_{t-t_0} \ , \tag{8.2}$$

where
$$\delta_{t-t_0} = \frac{([x_s(t), y_s(t), z_s(t)] - [x_s(t_0), y_s(t_0), z_s(t_0)]) \cdot \mathbf{n}}{cT} \ , \qquad (8.3)$$
being $[x_s(t), y_s(t), z_s(t)]$ the satellite position at the time instant t, $[x_s(t_0), y_s(t_0), z_s(t_0)]$ the satellite position at the time instant t_0 and T the pulsar period.

8.3 Software Structure

The five scripts constituting PODS are:

1. *PODS_executable*: this script is the Python file to be executed to start PODS. In this file, the user is able to define the true and the guess orbit along with all of the parameters related to the mission e.g. the number of telescopes and their characteristics (i.e. effective area and field-of-view), dark counts of the detector, clock error parameters and the observation schedule. The photons ToAs are generated in this script through Scipy's *Poisson* method.

2. *estimation*: this script contains the methods for the satellite state estimation (i.e. the batch least squares filter) and the subroutine to estimate the clock error parameters only.

3. *pulsar_range*: this script contains the class *PulsarRange*, which extends the Orekit's *AbstractMeasurement* class. The *theoreticalEvaluation* method performs the phase alignment of the photons ToAs and folds them to reconstruct the pulsar signal. Then, after the PAT estimation of the reconstructed signal, the (*O-C*) coefficients are computed to form the observation residuals.

4. *pulsar_utilities*: this script contains the methods for the folding and binning tasks along with the methods providing the user with the pulsar analytical templates.

5. *PAT_estimation*: this script contains the methods allowing to estimate the PAT of a pulsar signal. Both the steepest zero crossing technique and the MLE are implemented.

Tab. 8.2 shows an example for the simulation settings which can be set in PODS.

Table 8.2: Simulation example.

Force type	Pulsar signals generation	Orbit determination
gravitational	Sun (point mass attraction)	Sun (point mass attraction)
	Earth (EIGEN-6S4 Holmes-Featherstone attraction 6×6)	Earth (EIGEN-6S4 Holmes-Featherstone attraction 4×4)
	Moon (point mass attraction)	Moon (point mass attraction)
non-gravitational	Solar Radiation Pressure, box-wing model, 8 m^3 box with 20 m^2 solar panels. $\alpha_a = 0.9$, $\alpha_r = 0.1$.	Solar Radiation Pressure, cannonball model, 12 m^2 cross section, $\alpha_r = 0.2$
Simulation details		
estimated parameters		position, velocity, clock bias and clock drift
least squares optimizer		Levenberg-Marquardt
initial position (m)	(-5.818621509E7, 5.37299641E7, 5.40116157E7)	(-5.81743744E7, 5.37287364E7, 5.40037539E7)
initial velocity (m/s)	(-2110.93851224, 210.82792335, 210.23643338)	(-2110.93656044, 210.82538473, 210.2383837)
clock bias (s)	1e-5	3e-2
clock drift (s/s)	1e-11	4e-13
initial date (UTC)		Nov 8, 2025 23:22:07.1
integrator		Dormand-Prince 853, step $\in$ (0.1, 10) s
reference frame		International Celestial Reference Frame
observed pulsars		Crab

Chapter 9

Results

9.1 Clock Error Estimation Experiment with Real Pulsar Data

This section discusses the results of the estimation of the Aqueye+ reference oscillator error (bias and drift), using one hour of observation data of the Crab pulsar performed at the Copernicus telescope in Asiago, by exploiting the stability of the observed optical signal. Aqueye+ can time tag single photons detected from the observed optical target with an accuracy of a few hundreds of picoseconds [35] and refer them to Coordinated universal Times (UTC) with an accuracy below the nanosecond. For doing this, the instrument adopts a Stanford Rubidium clock FS725 as reference oscillator and a Mini-T Trimble GPS receiver (whose clock is steered by the GPS signal and maintained within an error of a few nanoseconds) for correcting the oscillator drift. The time steering of the rubidium oscillator is not performed by providing a Pulse Per Second (PPS) directly to the FS725 unit, but rather sending the PPS to the Time to Digital Converter (TDC) board, which also collects the signals from the Single Photon Avalanche Diode (SPAD) detectors. The time-tagged PPSs are then post-processed to determine the initial offset of the acquisition with reference to UTC and clock drift, allowing to correct the time tags of the photons and obtain the sub-nanosecond accuracy.

For this investigation, the collected photons ToAs are not corrected with the processing of the PPSs from the GPS, but rather they are used as a source to determine the reference oscillator error. The GPS receiver is also used to determine the reference point of the instrument installed at the Copernicus telescope, which in this analysis is assumed to be known. The Kalman filter described in Section 6.3 was used to estimate the reference clock bias (a_0) and drift (a_1). To test the algorithm, a 1-hour Crab pulsar observation performed on the night of 19 January 2018, starting at 20:24:43 UTC has been adopted.

To validate the algorithm, the estimation of a_0 and a_1 from the optical pulsar are compared with those estimated by the fit over the PPSs from the GPS receiver. For this observation, the GPS provided an estimation of $a_0 = 3.43 \times 10^{-9} \pm 1.49 \times 10^{-10}$ s and $a_1 = 4.061 \times 10^{-10} \pm 7.2 \times 10^{-14}$ s/s. Tab. 9.1 reports the values of a_0 and a_1 obtained by exploiting the optical signal of the Crab pulsar, with $\Delta t_k = 900$ s, as a function of the number of bins per period (50000, 100000, 200000 and 1000000).

Table 9.1: Clock bias and drift estimation results.

bins	a_0 (s)	a_1 (s/s)
50000	1.233E-06 $\pm$ 3.643E-07	1.618E-9 $\pm$ 2.101E-10
100000	1.699E-06 $\pm$ 5.644E-07	3.594E-10 $\pm$ 1.601E-10
200000	1.388E-06 $\pm$ 2.201E-06	4.623E-11 $\pm$ 1.303E-09
1000000	3.505E-06 $\pm$ 4.233E-06	4.447E-11 $\pm$ 2.514E-09

The values of a_0 estimated with the GPS and the pulsar signal differ because of a bias between the pulsar and GPS reference times. This bias defines the time shift to be applied by a pulsar user to be referred to the GPS time or UTC. A similar parameter shall be also provided among the pulsar timing parameters, in order to synchronize the user to a selected terrestrial

reference time frame.

It can be seen that in the case of 100000 bins the estimated clock drift differs of 4.66×10^{-11} s/s from that estimated by the GPS receiver. The reported results remark that the number of phase bins in which the pulsar signal is divided into is a fundamental parameter of the navigation system, which has to be chosen depending on the mission requirements. Generally speaking, a larger number of phase bins provides a better timing resolution, but at the expense of longer observations to achieve a given SNR. In the reported case in which increasing the number of phase bins worsen the accuracy in the clock error estimation, a longer observation would have been necessary for taking advantage of a larger number of phase bins. At the same time, also choosing a lower number of bins (i.e. 50000) does not improve the clock error estimation accuracy.

9.2 Optical Pulsar-based Orbit Determination and Time Synchronization for Spacecraft in Cislunar Near Rectilinear Halo Orbit

9.2.1 Near Rectilinear Halo Orbits

Near Rectilinear Halo Orbits (NRHOs) are gaining more and more traction as fundamental paths for future deep-space missions; for instance, NRHOs have been deemed suitable for the Moon-orbiting station Lunar Gateway, the first ever extraterrestrial space station [53]. NRHOs were first identified in a simplified gravitational representation of the Earth-Moon system, i.e., the Circular Restricted Three Body Problem (CR3BP) [54]. In the CR3BP model, NRHOs are characterized by beneficial stability properties, allowing to maintain a satellite in a NRHO-like motion over a long duration while consuming few propellant resources. NRHOs show also favorable resonance properties that can be exploited for mission design and to avoid eclipses [55]. In this Thesis, an Earth-Moon L2 NRHO is considered.

Perfectly periodic in the Earth-Moon CR3BP frame, an Earth-Moon NRHO can be simulated starting from an initial satellite state given in the CR3BP frame [55]. In the literature, many approaches have been proposed to find an initial satellite state leading to a (quasi-)ballistic NRHO. Common approaches are the forward/backward shooting methods, which forward/backward propagate the satellite orbit from a set of patch points (i.e. solutions of the Earth-Moon CR3BP) constraining it between each pair of points. The patch points act thus as orbital constrains leading to a (quasi-)ballistic trajectory passing through them [54].

NRHOs are a subset of the Earth-Moon L1 and L2 halo orbits, characterized by close passage over one of the lunar poles [53]. If the satellite apolune lies over the lunar North Pole, the NRHO is named Northern NRHO, while it is named Southern NRHO if the apolune lies over Moon's South Pole. An L2 Southern NRHO is considered in this case (Fig. 9.1), whose initial state is the one proposed in [55]. As from [55], the period of such an orbit is of about seven days.

9.2.2 Orbit Determination Results

As a first orbit determination example, the positioning accuracy of the proposed SNOP system is evaluated considering both range and Doppler measurements from the Crab pulsar only (Fig. 9.2). A telescope with an area of 0.07 m^2 and a field-of-view of 0.79 arcsec^2 has been considered. The number of light curves to be collected before running the navigation filter has been chosen to be $l = 30$ (hence leading to 60 measurements) where a single observation lasted 4000 s. Each signal is then partitioned into 1000 phase bins. The clock error is assumed to be negligible and only the satellite position and velocity are estimated. A Monte Carlo approach has been followed for the reported results.

Fig. 9.2 shows the obtained positioning error as a function of the observation time. The plot also provides the positioning error along the pulsar direction, the orbital plane and the direction given by the cross product be-
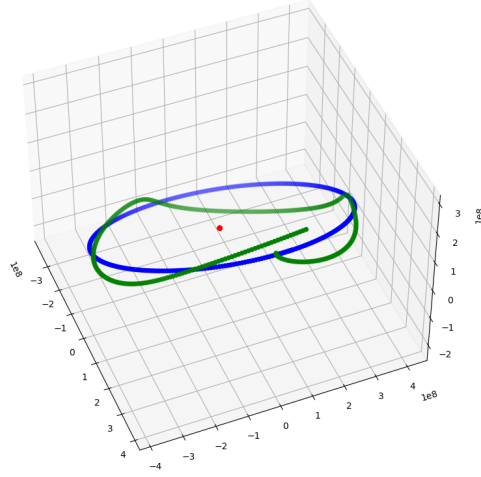
Figure 9.1: Simulated Earth-Moon L2 NRHO in the Earth-centered Earth-Sun rotating frame. The Earth is shown in red, the Moon's orbit in blue and the spacecraft orbit in green. The initial state is propagated up to 28 days. The measurement unit of the axes is in meters.

tween the two. The decrease of the positioning error becomes slower after about six days of observations, reaching about 700 m (average value) after 10 days. Clearly, since the measurements come from a single direction, a lower uncertainty is found along the line-of-sight of the pulsar. Similarly, Fig. 9.3 provides the error obtained in the velocity estimation.

For both the position and velocity estimation errors, it can be noticed that as the observation time increases, the addition of the Doppler measurement becomes less and less helpful. In fact, after about 5 days of observation, the accuracy of the navigation system considering both range and Doppler measurements does not show an improvement with respect to the range-only case.
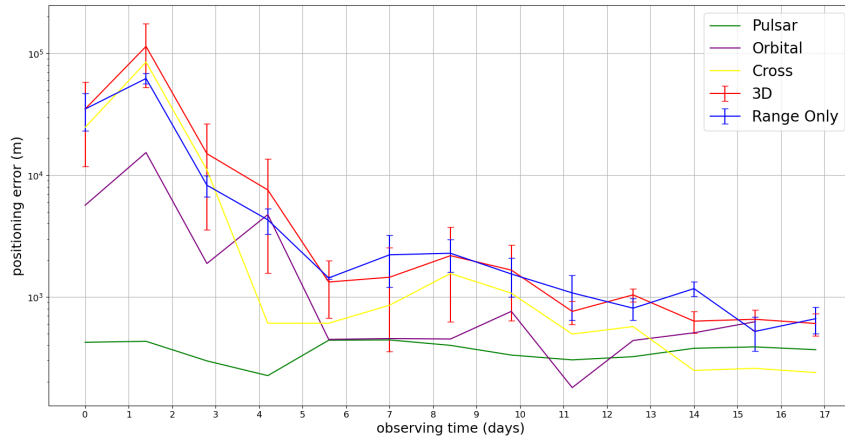
Figure 9.2: Positioning error as a function of the total observation time with both range and Doppler measurements observing the Crab pulsar.
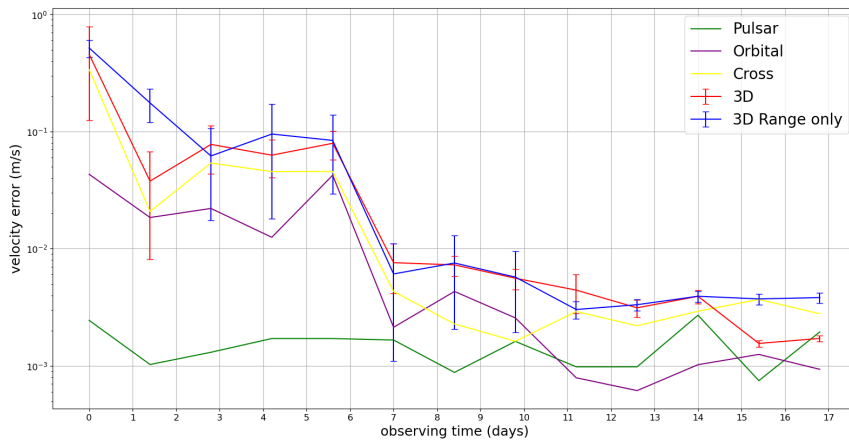

Figure 9.3: Velocity error as a function of the total observation time with both range and Doppler measurements observing the Crab pulsar.

9.2.3 Orbit Determination and Time Synchronization Results

The sequential-batch filter presented in this Thesis can be exploited to estimate the clock error parameters only. To estimate the upper limit in the clock error estimation accuracy, it is reasonable to study the performance of the clock error estimator when the true orbit is given to the satellite. In fact, if the satellite orbit is known, the phase alignment step is correctly carried out and the phase of the reconstructed signal is affected by the sole pulsar noise (i.e. photon shot noise and nebular background noise), which cannot be removed, and the clock error, which needs to be estimated. Tab. 9.2 reports the clock bias and drift estimation errors (one-sigma) obtained with a different number of range measurements l, where each light curve corresponds to a 4000 s long observation of the Crab pulsar. It should be noticed that if the guess orbit differs from the true orbit (i.e. in case of orbit determination error), the phase alignment task introduces errors in the signal phase reconstruction; in those cases, the achieved timing accuracy will always be worse than that shown in Tab. 9.2.

Table 9.2: Clock error estimation accuracy attainable with a telescope of area = 0.07 m^2 over a FoV = 0.79 arcsec^2 observing the Crab pulsar.

l	Bias estimation error (s)	Drift estimation error (s/s)
2	2.5e-06	5.2e-10
4	2.1e-06	2.0e-10
8	1.8e-06	6.2e-11
20	1.5e-06	1.9e-11
40	8.9e-07	8.8e-12

To study the performance of the navigation system while estimating both the satellite orbit and the clock error parameters, the two-stage strategy

presented in Section 6.4 has been exploited. In the first stage, the satellite collects l measurements and estimates the clock error parameters only. Once the clock bias and drift have been estimated, the satellite is responsible for correcting the photons' ToAs to compensate for the clock error contribution. Then, in the second stage, the corrected ToAs are exploited to construct the l measurements for determining the satellite orbit. Fig. 9.4 shows the positioning accuracy achieved by the proposed SNOP system with an initial clock error of 3.75e-06 s and 6.8e-11 s/s for the bias and drift components respectively.
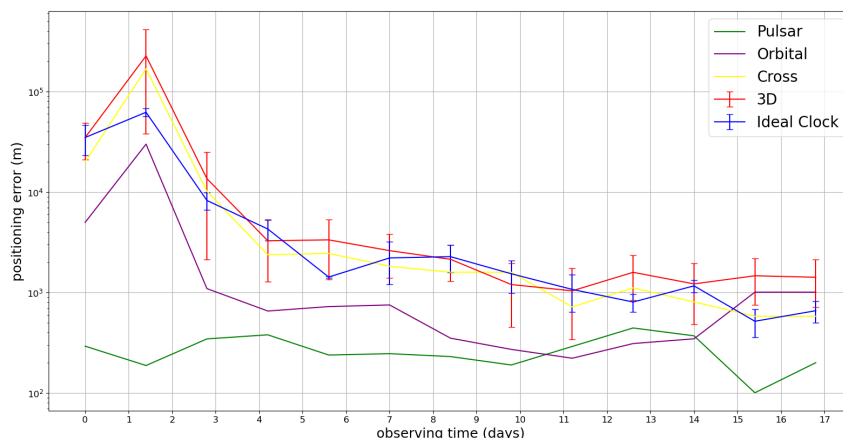

Figure 9.4: Positioning error as a function of the total observation time with both range and Doppler measurements observing the Crab pulsar.

It is clear from Fig. 9.4 that the presence of the clock error affects the system performance. In fact, if an average positioning error of about 700 m is obtained - neglecting the clock error - following 16 days of observations, the presence of non-zero bias and drift components (whose behavior is shown in Fig. 9.5) leads to an average error of about 1100 m after the same observation time.

To investigate the performance of a SNOP system simultaneously observing the Crab, Vela and B0540-69 pulsars, the following scenario has been
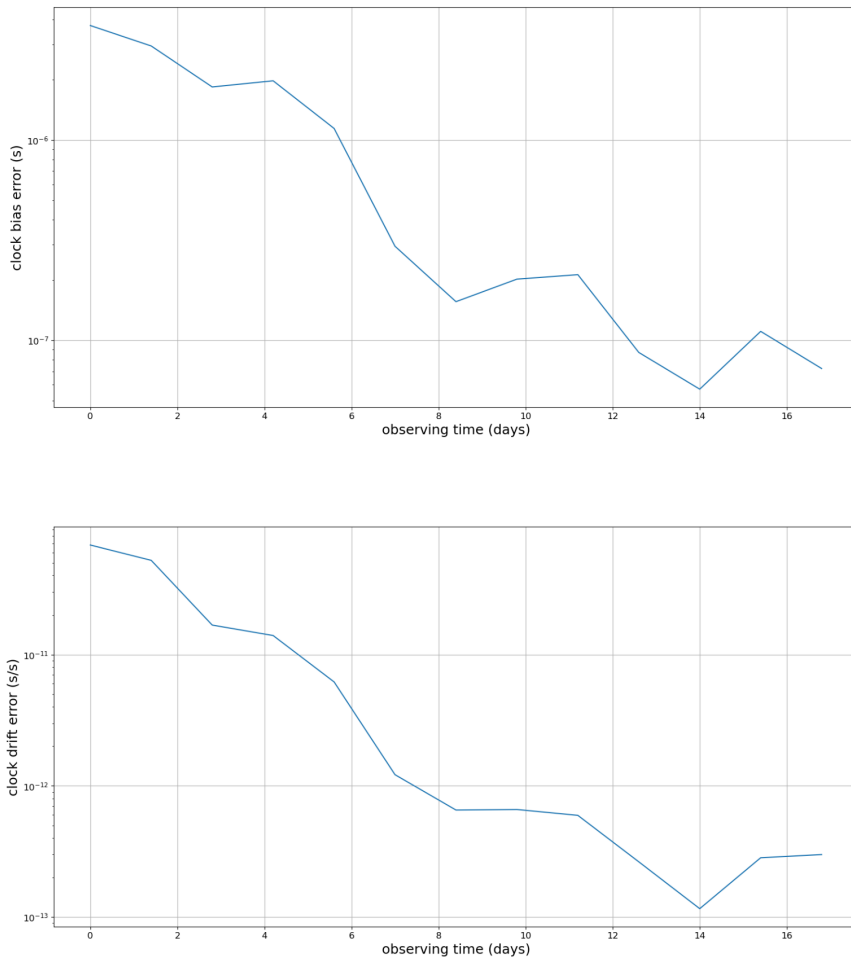
Figure 9.5: Clock bias (top) and drift (bottom) estimation errors as a function of the total observation time observing the Crab pulsar.

considered. Each pulsar is observed with a 0.3 m diameter telescope, over a field-of-view of 1 arcsec and the length of a single observation has been chosen equal to 4000 s for the Crab pulsar and 24000 s for the other sources. Fig. 9.6 shows the achieved positioning error as a function of the observation time. The navigation filter is executed every 1.4 days, hence leading to the collection of 30 light curves for the Crab pulsar and 5 for the Vela and B0540-69. Because of the long simulation times required for the multi-pulsar scenario, only range measurements have been considered for this analysis.
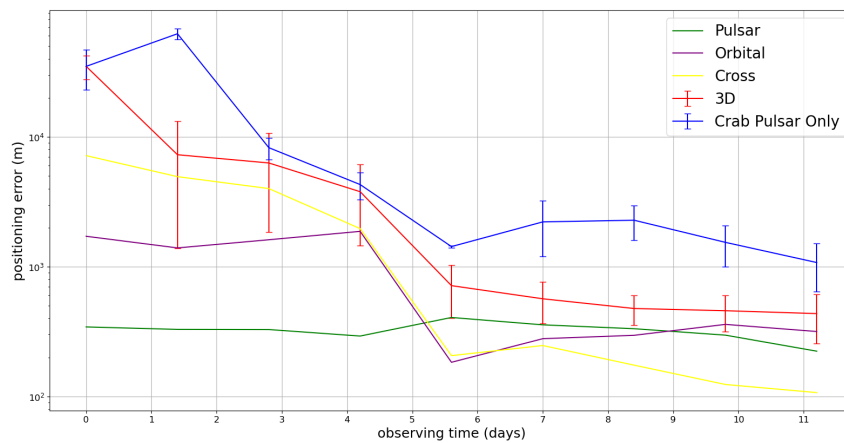

Figure 9.6: Positioning error as a function of the total observation time with range measurements only observing the three brightest optical pulsars.

It is clear from Fig. 9.6 that the addition of measurements coming from different directions decreases the positioning error faster. A mean positioning error of 435 m is obtained after 10 days of observation. Such a positioning error is expected to decrease further by increasing the amount of observations.

Chapter 10

Conclusions

This work investigated, for the first time ever, the exploitation of optical pulsars for deep-space navigation. Because of the low number of optical pulsars, no previous studies analyzed such a possibility in the past. Also several studies claimed that the achievable SNR would have not been sufficient for navigation purposes, neglecting the usage of optical pulsars for decades. Nevertheless, no research activity properly investigated the advantages optical pulsars could bring, in particular evaluating the SNR achievable by a narrow field-of-view system.

This Thesis accurately investigated the potential of optical pulsars, proposing the navigation techniques and the optical design for the navigation payload. The algorithms exploited for the analysis have been validated with both simulated and real data. Real observations of the Crab pulsar were made at the Asiago Observatory, while optical data for the B0540-69 and Vela pulsars from the New Technology Telescope were used to estimate the photon fluxes of these sources. The results prove that sub-km positioning accuracies can be obtained anywhere in the solar system with a payload whose size, weight and power are much less demanding with respect to the currently adopted X-ray systems. Moreover, all of the requirements of the system have been deemed achievable with present technologies. A proper analysis of the velocity estimation error has been performed, along with an

investigation on the on-board time synchronization performance achieved by the satellite. Optical pulsars could thus play a role in an Earth-independent orbit determination and time synchronization system which is particularly attractive for - but not limited to - deep space missions.

Chapter 11

Acknowledgements

Bibliography

[1] Bauer, F.H., Hartman, K. and Lightsey, E.G. *Spaceborne gps current status and future visions*, Aerospace Conference, 1998 IEEE Aerospace Conference Proceedings (Cat. No.98TH8339), Vol. 3, March 1998, pp. 195-208. https://doi.org/10.1109/AERO.1998.685798.

[2] Curkendall, D.W. and Border, J.S., *Delta-DOR: the one-nanoradian navigation measurement system of the deep space network history, architecture, and componentry*, Interplanetary Network Progress Report, Vol. 42-193, May 2013, pp. 1-46.

[3] Zoccarato, P., Larese, S., Naletto, G., Zampieri, L., Brotto, F., *Deep space navigation by optical pulsars*, Journal of Guidance, Control and Dynamics, 2023, 46(8)

[4] Downs, G. S., *Interplanetary Navigation Using Pulsating Radio Sources*, NASA 74N34150, 1974.

[5] Becker, W., Bernhardt, M. G., and Jessner, A., *Autonomous Spacecraft Navigation With Pulsars*, Acta Futura, Vol. 7, March 2013, pp. 11-28. https://doi.org/10.2420/AF07.2013.11

[6] Emadzadeh, A. A., and Speyer, J. L., *Navigation in Space by X-Ray Pulsars*, Springer, New York, 2011, pp. 13â33. https://doi.org/10.1007/978-1-4419-8017-5

[7] Zheng, S. J., Zhang, S. N. Lu, F. J., Wang, W. B., Gao, Y., Li, T. P. Song, L. M., Ge, M. Y., Han, D. W., Chen, Y., Xu, Y. P., Cao, X. L.,

Liu, C. Z., Zhang, S., Qu, J. L., Chang, Z., Chen, G., Chen, L., Chen, T. X., Chen, Y. B., Chen, Y. P., Cui, W., Cui, W. W., Deng, J. K., Dong, Y. W., Du, Y. Y., Fu, M. X., Gao, G. H., Gao, H., Gao, M., Gu, Y. D., Guan, J., Gungor, C., Guo, C. C., Han, D. W., Hu, W., Huang, Y., Huo, J., Ji, J. F., Jia, S. M., Jiang, L. H., Jiang, W. C., Jin, J., Jin, Y. J., Li, B., Li, C. K., Li, G., Li, M. S., Li, W., Li, X., Li, X. B., Li, X. F., Li, Y. G., Li, Z. J., Li, Z. W., Liang, X. H., Liao, J. Y., Liu, G. Q., Liu, H. W., Liu, S. Z., Liu, X. J., Liu, Y., Liu, Y. N., Lu, B., Lu, X. F., Luo, T., Ma, X., Meng, B., Nang, Y., Nie, J. Y., Ou, G., Sai, N., Shang, R. C., Sun, L., Tan, Y., Tao, L., Tao, W., Tuo, Y. L., Wang, G. F., Wang, J., Wang, W. S., Wang, Y. S., Wen, X. Y., Wu, B. B., Wu, M., Xiao, G. C., Xiong, S. L., Xu, H., Yan, L. L., Yang, J. W., Yang, S., Yang, Y. J., Zhang, A. M., Zhang, C. L., Zhang, C. M., Zhang, F., Zhang, H. M., Zhang, J., Zhang, Q., Zhang, T., Zhang, W., Zhang, W. C., Zhang, W. Z., Zhang, Y., Zhang, Y., Zhang, Y. F., Zhang, Y. J., Zhang, Z., Zhang, Z., Zhang, Z. L., Zhao, H. S., Zhao, J. L., Zhao, X. F., Zhu, Y., Zhu, Y. X. and Zou, C. L., *In-orbit Demonstration of X-Ray Pulsar Navigation with the Insight-HXMT Satellite*, The Astrophysical Journal Supplement Series, Vol. 244, September 2019. https://doi.org/10.3847/1538-4365/ab3718

[8] Sheikh, S. I., Pines, D. J., Ray, P. S., Wood, K. S., Lovellette M. N. and Wolff, M. T., *Spacecraft Navigation Using X-Ray Pulsars*, Journal of Guidance, Control and Dynamics, Vol. 29, January 2006, pp. 49-63. https://doi.org/10.2514/1.13331

[9] Sheikh, S.I., Pines, D.J., *Recursive estimation of spacecraft position and velocity using X-ray pulsar time of arrival measurements*, Navigation: Journal of The Institute of Navigation, Vol. 53, Fall 2006, pp. 149â166. https://doi.org/10.1002/j.2161-4296.2006.tb00380.x

[10] Sala, J., Urruela, A., Villares, X., Estalella, R., and Paredes, J. M., *Feasibility Study for a Spacecraft Navigation System Relying on Pulsar*

Timing Information, European Space Agency Advanced Concepts Team ARIADNA, Rept. 03/4202, Noordwijk, The Netherlands, June 2004.

[11] Mitchell, J. W., Winternitz, L. B, Hassouneh, M. A., Price, S. R., Semper, S. R., Yu, W. H., Ray, P. S., Wolff, M. T., Kerr M., Wood, K. S., Arzoumanian, Z., Gendreau, K. C., Guillemot, L., Cognard, I., Demorest, P., *SEXTANT X-Ray Pulsar Navigation Demonstration: Initial On-Orbit Results*, 41st Annual American Astronautical Society, Feb 2018. Report No.:TN51848

[12] Cacciatore, F., $G\tilde{A}^3 mezRuiz, V., Taubmann, G., Munoz, J., Hermosn, P., Sciarra, M., Saco, M, Rea, N., Hernanz, M., Parent, E., Vandersteen, J., PODIUM:A Pu$ $22, B6, IPB, 2023.$

[13] Christian, J. A., *Optical Navigation Using Planetâs Centroid and Apparent Diameter in Image*, Journal of Guidance, Control and Dynamics, Vol. 38, February 2015, pp. 192-204. https://doi.org/10.2514/1.G000872

[14] Franzese, V., Di Lizia, P. and Topputo, F., *Autonomous Optical Navigation for the Lunar Meteoroid Impacts Observer*, Journal of Guidance, Control and Dynamics, Vol. 42, July 2019, pp. 1579-1586. https://doi.org/10.2514/1.G003999

[15] Lyne, A., and Graham-Smith, F., *Pulsar Astronomy*, 3rd ed., Cambridge Univ. Press, Cambridge, England, U.K., 2005, pp. 1â13, 90â100. https://doi.org/10.1017/CBO9780511844584

[16] Wertz, J. R., *Spacecraft Attitude Determination and Control*, Kluwer (1978)

[17] Hauschild, A., Montenbruck, O., Steigenberger, P., Martini, I., Fernandez-Hernandez, I, *Orbit determination of Sentinel-6A using the Galileo high accuracy service test signal*, GPS Solut 26, 120 (2022). https://doi.org/10.1007/s10291-022-01312-5

[18] Darugna, F., Casotto, S., Bardella, M., Sciarratta, M., Zoccarato, P, *Sub-Decimeter Onboard Orbit Determination of LEO Satellites Using SSR Corrections: A Galileo-Based Case Study for the Sentinel-6A Satellite*, Remote Sens. 2022, 14, 6121. https://doi.org/10.3390/rs14236121

[19] P. Cappuccio et al., *Report on First Inflight Data of BepiColombo's Mercury Orbiter Radio Science Experiment*, in IEEE Transactions on Aerospace and Electronic Systems, vol. 56, no. 6, pp. 4984-4988, Dec. 2020, doi: 10.1109/TAES.2020.3008577

[20] Lawrence, A., An Outline of Inertial Navigation, *Modern Inertial Technology, Springer*, pages 4-24 (1998)

[21] Deng, X.P., Hobbs, G., You, X. P., Li, M. T., Keith, M. J., Shannon, R. M., Coles, W., Manchester, R.N., Zheng, X.Z. Y, Gao, D., Wu, X., and Chen, D., *Interplanetary spacecraft navigation using pulsars*, Advances in Space Research, 52(9): 1602-1621 (Nov 2013)

[22] Baade, W., and Zwicky, F., *Remarks on super-novae and cosmic rays*, Phys. Rev., 46:76-77 (Jul 1934)

[23] Shapiro, S. L., and Teukolsky, S. A., *Book-Review - Black-Holes White Dwarfs and Neutron Stars*. Journal of the British Astronomical Association, 93(6):276 (Oct 1983)

[24] Hewish, A., Bell, J., Pilkington, J.D.H, Scott, P.F., and Collins, R. A., *Observation of a Rapidly Pulsating Radio Source*, Nature (1968).

[25] Gold, T., *Rotating Neutron Stars as the Origin of the Pulsating Radio Sources*, Nature, 218(5143):731-732 (May 1968)

[26] Mignani, R. P., Caraveo, P. A., and Bignami, G. F., *Optical observations of pulsars: the ESO contribution*, The Messenger, 99:22-26 (Mar 2000)

[27] Cocke, W. J., Disney, M. J., and Taylor, D. J., *Discovery of Optical Signals from Pulsar NP 0532*, Nature (1969)

[28] Wallace, P. T., Peterson, B. A., Murdin, P. G., Danziger, I. J., Manchester, R. N, Lyne, A. G., Goss, W. M., Smith, F. G., Disney, M. J., Hartley, K. F., Jones, D. H., and Wellgate, G. W., *Detection of optical pulses from the VELA PSR*, Nature (Apr 1977)

[29] Ghosh, P., and Lamb, F. K., *Diagnostics of disk-magnetosphere interaction in neutron star binaries*, NASA STI/Recon Technical Report A, 93:487-510 (Jan 1992)

[30] Cadez, A., Zampieri, L., Barbieri, C., Calvani, M., Naletto, G., Barbieri, M., and Ponikvar, D., *What brakes the Crab pulsar?*, 587 (Mar 2016)

[31] Hobbs, G., Lyne, A., and Kramer, M., *An analysis of the timing irregularities for 366 pulsars*, 402(2):1027-1048 (Feb 2010)

[32] Zampieri, L, A. Cadez, C. Barbieri, G. Naletto, M. Calvani, M. Barbieri, E. Verroi, P. Zoccarato, and T. Occhipinti, *Optical phase coherent timing of the Crab nebula pulsar with Iqueye at the ESO New Technology Telescope*, 439(3):2813-2821, (Apr 2014)

[33] Massaro, E., Campana, R., Cusumano, G. and Mineo, T., *The optical to gamma-ray emission of the Crab pulsar: a multicomponent model*, Astronomy and Astrophysics, Vol. 459, Dec. 2006, pp. 859-870. https://doi.org/10.1051/0004-6361:20065118

[34] Ambrosino, F., Papitto, A., Stella, L., Meddi, F., Cretaro, P., Burderi, L., Di Salvo, T., Israel, G. T., Ghedina A., Di Fabrizio, L., Riverol, L., *Optical pulsations from a transitional millisecond pulsar*, Natural Astronomy, Vol. 1, October 2017, pp. 854â858. https://doi.org/10.1038/s41550-017-0266-2

[35] Zampieri, L., Burtovoi, A., Fiori, M., Naletto, G., Spolon A., Barbieri, C., Papitto A., and Ambrosino, F., *Precise optical timing of PSR J1023+0038, the first millisecond pulsar detected with Aqueye+ in Asi-*

ago, Monthly Notices of the Royal Astronomical Society, Vol. 485, March 2019, pp. L109-L113. https://doi.org/10.1093/mnrasl/slz043

[36] Ambrosino, F., Miraval Zanon, A., Papitto, A., Coti Zelati, F., Campana, S., DâAvanzo, P., Stella, L., Di Salvo, T., Burderi, L., Casella, P., Sanna, A., De Martino, D., Cadelano, M., Ghedina, A., Leone, F., Meddi, F., Cretaro, P., Baglio, M. C., Poretti, E., Mignani, R. P., Torres, D. F., Israel, G. L., Cecconi, M., Russell, D. M., Gonzalez Gomez, M. D., Riverol Rodriguez, A. L., Perez Ventura, H., Hernandez Diaz, M., San Juan, J. J., Bramich, D. M., and Lewis, F., *Optical and ultraviolet pulsed emission from an accreting millisecond pulsar*, Nature Astronomy, Vol 5, February 2021, pp. 552-559. https://doi.org/10.1038/s41550-021-01308-0

[37] Fermi LAT Collaboration, *An extremely bright gamma-ray pulsar in the Large Magellanic Cloud*, Science, Vol. 350, November 2015, pp.801-805. https://doi.org/10.1126/science.aac7400

[38] Pavlov, G. G., Zavlin, V. E., Sanwal, D., Burwitz, V., and Garmire, G. P., *The X-ray Spectrum of the Vela Pulsar Resolved with the Chandra X-ray Observatory*, The Astrophysical Journal, Vol. 552, May 2020, pp. L129âL133. https://doi.org/10.1086/320342

[39] Golshan, A.R., and Sheikh, S.I., *On Pulsar Phase Estimation and Tracking of Variable Celestial X-ray Sources*, 63rd Annual Meeting of Institute of Navigation (ION), Cambrige, MA, USA (April 2007)

[40] Edwards, R. T., Hobbs, G. B., Manchester, R. N., *TEMPO2: a New Pulsar Timing Package. II: The timing model and precision estimates*, Monthly Notices of the Royal Astronomical Society, Vol. 372, Nov 2006, pp. 1549-1574. https://doi.org/10.1111/j.1365-2966.2006.10870.x

[41] Zampieri, L., Cadez, A., Barbieri, C., Naletto, G., Calvani, M., Barbieri, M., Verroi, E., Zoccarato, P., and Occhipinti, T., *Optical phase coherent*

timing of the Crab nebula pulsar with Iqueye at the ESO New Technology Telescope, Monthly Notices of the Royal Astronomical Society, Vol. 439, February 2014, pp. 2813-2821. https://doi.org/10.1093/mnras/stu136

[42] Germana', C., Zampieri, L., Barbieri, C., Naletto, G., Cadez, A., Calvani, M., Barbieri, M., Capraro, I., Di Paola, A., Facchinetti, C., Occhipinti, T., Possenti, A., Ponikvar, D., Verroi, E., and Zoccarato, P., *Aqueye optical observations of the Crab Nebula pulsar*, Astronomy & Astrophysics, Vol 548, December 2012. https://doi.org/10.48550/arXiv.1210.1796

[43] Kaplan, E., Hegarty, C., *Understanding GPS: principles and applications*, Artech House, 2006.

[44] Mengfan, X., Dongliang, P., Haifeng, S., Han, S., Yunfei, G., Jiâan, L., Zhikun, C., *X-ray pulsar navigation based on two-stage estimation of Doppler frequency and phase delay*, Aerospace Science and Technology, 2021, 110.

[45] Spolon, A., Zampieri, L., Burtovoi, A., Naletto, G., Barbieri, C., Barbieri, M., Patruno, A., and Verroi, E., *Timing analysis and pulse profile of the Vela pulsar in the optical band from Iqueye observations*, Monthly Notices of the Royal Astronomical Society, Vol. 482, September 2018, pp. 175-183. https://doi.org/10.1093/mnras/sty2605

[46] Gradari, S., Barbieri, M., Barbieri, C., Naletto, G., Verroi, E., Occhipinti, T., Zoccarato, P., Germana', C., Zampieri, L., and Possenti, A., *The optical light curve of the Large Magellanic Cloud pulsar B0540-69 in 2009*, Monthly Notices of the Royal Astronomical Society, Vol. 412, April 2011, pp. 2689-2694. https://doi.org/10.1111/j.1365-2966.2010.18103.x

[47] Zeni, G., *Telescope assembly for a pulsar spacecraft navigation system*, Master's Thesis, Department of Industrial Engineering, University of Padova, 2020.

[48] Bosco, A., Bacchetta, A., Saponara, M., Saavedra Criado, G., *Euclid pointing performance: operations for the Fine Guidance Sensor reference star catalogue*, SpaceOps Conferences, 28 May - 1 June 2018.

[49] Bowman, D. M., Vandenbussche, B., Sana, H., Tkachenko, A., Raskin, G., Delabie, T., Vandoren, B., Royer, P., Garcia, S., Van Reeth, T., and the CubeSpec Collaboration, *The CubeSpec space missionI-1. Asteroseismology of massive stars from time-series optical spectroscopy: Science requirements and target list prioritisation*, Astronomy and Astrophysics, Vol. 658

[50] Ogiers, W., Ruythooren, K., Van Wichelen, K., Dendoncker, M., Kowaltschek, S. and Razgus, B., *FAINTSTAR: an intelligent single-chip sensor head for star trackers - prototype results*, CEAS Space Journal, Vol. 10, N. 4, Dec 2018.

[51] Maisonobe, L. et al., Orekit 11.3.2, Zenodo (2023)

[52] Zheng, S., Ge, M., Han, D., Wang, W., Chen, Y., Lu, F., Bao, T., Chai, J., Dong, Y., Feng, M., He, J., Huang, Y., Kong, M., Li, H., Li, L., Li, Z., Liu, J., Liu, X, Shi, X., L. Song, J. Sun, R. Wang, Y. Wang, X. Wen, B. Wu, H. Xiao, S. Xiong, H. Xu, M. Xu, J. Zhang, L. Zhang, L. Zhang, X. Zhang, Y. Zhang, Y. Zhao, and S. Zhang, *Test of pulsar navigation with POLAR on TG-2 space station*, Scientia Sinica Physica, Mechanica & Astronomica, 47(9):09950 (Sep 2017)

[53] Chavers, G. and Suzukib, N. and Smithc, M. and Watson-Morgan, L. and Clarke, S. W. and Engelund, W. C. and Aitchison, L. and McEniry, S. and Means, L. and DeKlotz, M. and Jackson, S., *NASA's Human Lunar Landing Strategy*, International Astronautical Congress, 70, 54732, 2019.

[54] Zimovan, E. M. and Howelly, K. C. and Davis, D. C., *Near Rectilinear Halo Orbits and Their Application in Cislunar Space*, IAA Conference on Dynamics and Controls of Space System, 3, 2017.

[55] Williams, J. and Lee, D. E. and Whitley, R. J. and Bokelmann, K. A. and Davis, D. C. and Berry, C. F., *Targeting Cislunar Near Rectilinear Halo Orbits for Human Space Exploration*, AAS/AIAA Space Flight Mechanics Meeting, 2017.